

# Earth and Space Science



## RESEARCH ARTICLE

10.1029/2024EA003617

### Key Points:

- We determined focal mechanisms and centroid depths for 28 deep-focus earthquakes along the Peru-Brazil border from 2014 to 2022
- Deep-focus earthquakes in South America are possibly nucleated from transformational faulting in a metastable olivine wedge
- Depth distribution of deep-focus earthquakes is possibly controlled by the subduction of the aseismic ridges and flat subduction

### Supporting Information:

Supporting Information may be found in the online version of this article.

### Correspondence to:

G. S. Leite Neto,  
[leitenetogs@gmail.com](mailto:leitenetogs@gmail.com)

### Citation:

Leite Neto, G. S., Juliã, J., & Prieto, G. A. (2024). Deep-focus earthquake mechanisms at the subducting Nazca plate (Peru-Brazil border): Cold slab behavior in a warm plate. *Earth and Space Science*, 11, e2024EA003617. <https://doi.org/10.1029/2024EA003617>

Received 4 MAR 2024

Accepted 12 SEP 2024

### Author Contributions:

**Conceptualization:** G. S. Leite Neto, J. Juliã

**Data curation:** G. S. Leite Neto

**Formal analysis:** G. S. Leite Neto

**Funding acquisition:** J. Juliã

**Investigation:** G. S. Leite Neto

**Methodology:** G. S. Leite Neto

**Project administration:** J. Juliã

**Software:** G. S. Leite Neto

**Supervision:** J. Juliã

**Validation:** J. Juliã, G. A. Prieto

**Visualization:** G. S. Leite Neto

**Writing – original draft:** G. S. Leite Neto

**Writing – review & editing:** J. Juliã,

G. A. Prieto

© 2024. The Author(s).

This is an open access article under the terms of the [Creative Commons Attribution-NonCommercial-NoDerivs License](https://creativecommons.org/licenses/by/4.0/), which permits use and distribution in any medium, provided the original work is properly cited, the use is non-commercial and no modifications or adaptations are made.

## Deep-Focus Earthquake Mechanisms at the Subducting Nazca Plate (Peru-Brazil Border): Cold Slab Behavior in a Warm Plate

G. S. Leite Neto<sup>1</sup> , J. Juliã<sup>1,2</sup> , and G. A. Prieto<sup>3</sup> 

<sup>1</sup>Programa de Pós-Graduação em Geodinâmica e Geofísica, Universidade Federal do Rio Grande do Norte, Natal, Brazil,

<sup>2</sup>Departamento de Geofísica, Universidade Federal do Rio Grande do Norte, Natal, Brazil, <sup>3</sup>Departamento de Geociencias, Universidad Nacional de Colombia, Bogotá, Colombia

**Abstract** We calculate focal mechanisms and centroid depths for deep-focus earthquakes (DFEs) along the Peru-Brazil border. We obtained a total of 28 focal solutions for events with magnitudes between 4.2 and 7.5 Mw and occurring between 2014 and 2022. Focal mechanisms indicate predominance of normal faulting, demonstrating a rather uniform down-dip compression (DDC) regime within the plate. The orientations of the nodal planes suggest that earthquakes tend to occur along faults parallel to the local slab strike, although other fault types are documented. Stress orientations derived from the focal mechanisms agree with patterns expected if faulting were initiated by transformational faulting on a metastable olivine wedge (MOW) under DDC. Centroid depths range between 557 and 659 km, defining a narrow seismic zone within the lower portion of the subducting plate and an aseismic upper portion. We suggest that DFEs nucleate through transformational faulting within a narrow MOW preserved at a colder slab segment right above the lower mantle and juxtaposed to a shallower, warmer segment at around 500 km depth. This thermal complexity was possibly produced through flat subduction initiated by the subduction of the Nazca Ridge. We speculate that subduction of other aseismic ridges is possibly controlling the thermal state of the Nazca slab as a whole and, consequently, the depth distribution of DFEs along the South America subduction front.

**Plain Language Summary** Aiming to better understand the dynamics of deep earthquakes, we studied mechanisms and depths for deep-focus earthquakes (DFEs) from 2014 to 2022 at the Peru-Brazil border. We determined focal mechanisms for 28 events, which indicate the predominance of normal faulting and demonstrate that the Nazca plate is under down-dip compression (DDC). Stresses from these mechanisms agree with patterns expected if faulting were initiated by the transformational faulting mechanism on a metastable olivine wedge (MOW) under DDC. Events' depths ranged from 557 to 659 km, defining a narrow seismic zone within the plate. We suggest that DFEs are nucleating through transformational faulting in a narrow MOW preserved at a colder slab segment right above the lower mantle and connected to a warmer segment at around 500 km depth. Thermal complexity possibly resulted from the flat subduction associated with the Nazca Ridge. We speculate that subduction of other aseismic ridges is possibly controlling the thermal state of the Nazca slab as a whole and, consequently, the depth distribution of DFEs along the South America subduction front.

## 1. Introduction

DFEs ( $d > 300$  km) are limited to a few subduction zones worldwide and are generally confined within the cold core of subducting oceanic plates. Due to the extreme pressure and temperature conditions in which these events take place, brittle failure as we know it should be inhibited (Houston, 2015); thus, deep earthquakes must be mechanically different from ordinary shallow earthquakes and have a physical mechanism that accounts for faulting at such great depths. Although several physical processes have been identified, this mechanism remains largely unresolved due to limitations in each proposed mechanism to explain all observations (Frohlich, 1989, 2006; Houston, 2015; Zhan, 2020).

The mechanisms traditionally proposed for DFEs include transformational faulting (Green & Burnley, 1989; Green & Marone, 2002; Green & Zhou, 1996) and thermal runaway (Kanamori et al., 1998; Ogawa, 1987). Transformational faulting is basically a high-pressure, self-organizing shear instability that requires an exothermic phase change to nucleate small anti-cracks. Those are microscopic lenses filled with superplastic and denser material that form and grow under compressive stress regimes, the instability resulting from the

superplastic filling (Green & Burnley, 1989; Green & Marone, 2002; Green & Zhou, 1996). Transformational faulting would require DFEs to nucleate at the relatively lower temperatures inside subducting oceanic plates, where olivine can be metastably preserved down to mantle transition zone (MTZ) depths within the so-called Metastable Olivine Wedge (MOW) (e.g., Bina et al., 2001; Devaux et al., 2000). Under this hypothesis, the expected exothermic transformations from olivine to wadsleyite (~410 km) and from wadsleyite to ringwoodite (~520 km) could be responsible for triggering transformational faulting, thus explaining DFEs confinement around MTZ depths (Green & Zhou, 1996; Houston, 2015; Zhan, 2020). Based on laboratory observations in Ge-olivine, Gasc et al. (2022) suggested that, once transformational faulting is initiated, faulting can propagate beyond the MOW through melting-assisted processes. They also noted that transformational faulting would have to take place within a narrow range of temperatures (600–700°C) in both cold and warm slabs. Moreover, this range would depend on strain rate and favor nucleation along the borders of the MOW, possibly explaining the existence of double seismic zones and higher *b*-values in cold plates.

An important physical constraint is that transformational faulting would require that olivine remains sufficiently dry within the oceanic lithosphere, as its transformation into denser polymorphs is catalyzed in the presence of even small amounts of water (e.g., Du Frane et al., 2013; Hosoya et al., 2005; Kubo et al., 1998). Interestingly, recent studies have pointed out that olivine can remain dry within the MTZ thanks to the presence of hydrous phase A under water-undersaturated conditions (Ishii & Ohtani, 2021), and thus that water may actually play an important role in promoting earthquake nucleation in the MOW (e.g., Mao et al., 2022).

Thermal runaway, on the other hand, would be the result of a positive thermal feedback between the heat generated by shearing and viscosity reduction, which might or might not culminate in melting (Green & Marone, 2002; Zhan, 2020). This mechanism, however, seems to lack the ability to nucleate ruptures by itself (Green & Marone, 2002; Kelemen & Hirth, 2007) and thus is often regarded as an auxiliary mechanism to transformational faulting that extends DFEs beyond the MOW (e.g., Zhan, 2017). The very low seismic efficiency found for the 1994 Mw 8.2 Bolivia earthquake is generally invoked as strong evidence for the co-existence of such a dissipative process in the genesis of this large DFE (Kanamori et al., 1998).

Slab temperature plays a fundamental role in the ability of these mechanisms to trigger DFEs (Billen, 2020; Houston, 2015). As mentioned above, transformational faulting is strongly linked to the preservation of a MOW within the subducting slab, which is in turn dependent on the slab's thermal state through the dependence of phase transformation rates on temperature (Green & Marone, 2002; Green & Zhou, 1996). The slab's thermal state is often described through the thermal parameter, an oversimplification of its thermal structure obtained as the product of age, dip, and convergence rate (Frohlich, 2006; Kirby et al., 1991). According to this parameter, only the coldest plates (e.g., Tonga) are expected to retain a MOW down to the base of the MTZ (~660 km) (Devaux et al., 1997; Mosenfelder et al., 2001). Despite that, earthquakes at such depths are also observed in warmer slabs (Devaux et al., 1997; Houston, 2015). To account for this limitation, transformational faulting on a metastable enstatite wedge (MEW) has been proposed, which could explain earthquakes over a depth range beyond that of the MOW (Green & Zhou, 1996; Högrefe et al., 1994). Thermal runaway, on the other hand, naturally requires sufficiently high temperatures to allow for sufficient viscosity reduction and subsequent instability (Green & Marone, 2002; Houston, 2015). Thermally induced instability could explain dissipative events occurring predominantly—but not exclusively—in warmer slabs (Tibi et al., 2003; Zhan, 2020; Zhan et al., 2014). In this sense, bigger ruptures would be initiated by transformational faulting in a thin MOW in warmer slabs and further propagate through thermal runaway (Zhan, 2017).

Nonetheless, because the slab thermal parameter is an oversimplification, assessing the viability of the mechanisms might not be as straightforward. For young, slow lithosphere, for example, deep-focus seismicity ( $d > 300$  km) is generally absent (Myhill, 2013; Wortel, 1982); yet, the Nazca plate, which clearly falls at the warm end of the thermal parameter spectrum of subducting slabs, does host deep-focus ruptures (Houston, 2015). It has been proposed that the subducting Nazca slab might have a composite thermal structure consisting of a cold, deeper portion attached to a warm, shallower portion—with the transition possibly happening at 500 km depth—and that the cold portion of this composite structure might meet the requirements for hosting a MOW and trigger DFEs (Collier & Helffrich, 2001; Engebretson & Kirby, 1992; Kirby et al., 1995; Okal & Bina, 1994; Zahradník et al., 2017). Moreover, while this bottom segment may have remained cold enough to effectively retain olivine metastably to MTZ depths, olivine in the warmer segment may have been completely transformed aseismically near the nominal transformation depth, thus impeding metastability and explaining the prominent seismic gap

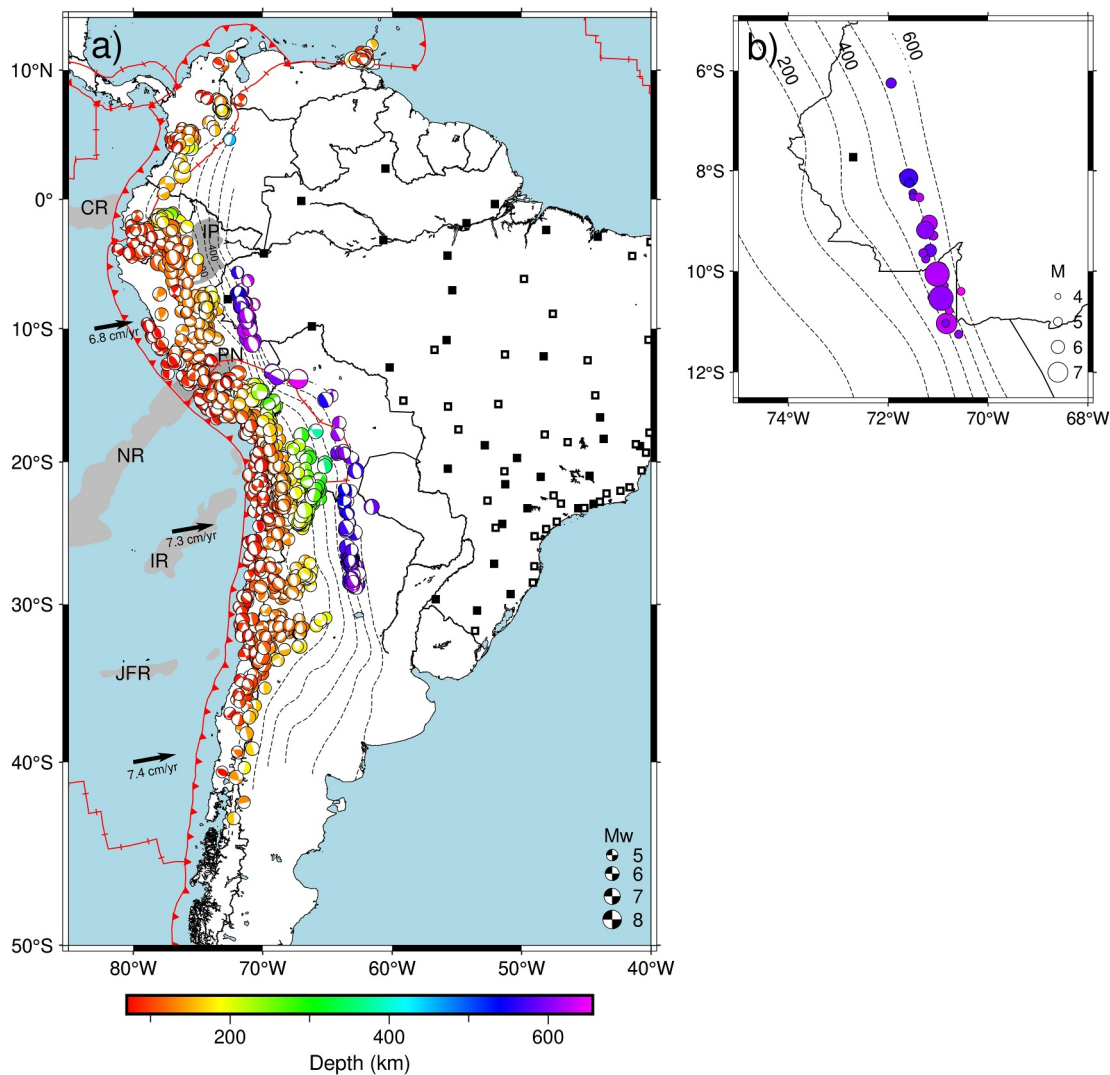


**Figure 1.** (a) Moment tensor solutions for deep earthquakes ( $d > 70$  km and  $M_w > 5$ ) in South America according to the GCMT catalog (1977–2022). The focal solutions in this map are colored by depth and sized by magnitude. Plate boundaries are from Bird (2003) and convergence rate of the Nazca plate in cm/yr are from DeMets et al. (2010). Contours from Slab 2 delineate the geometry of the subducting Nazca plate (Hayes et al., 2018). Main oceanic ridges in Nazca plate: CR—Carnegie Ridge, NR—Nazca Ridge, IR—Iquique Ridge and JFR—Juan Fernandez Ridge, are shown in light gray (Gutscher et al., 2000; Rosenbaum et al., 2005). The inferred continuation of the Nazca Ridge (PN) and location of the postulated Inca Plateau (IP) are drawn in dark gray (Bishop et al., 2017; Gutscher et al., 1999, 2000). Distribution of broadband stations from the Brazilian Seismic Network (RSBR) for different time periods are shown as open (1980–2013) and closed (2014–2022) squares; (b) 42 DFEs ( $d > 300$  km) within the period of 2014–2022 according to the USGS catalog.

between 300 and 500 km depth and the corresponding concentration of DFEs at depths larger than 500 km (Kirby et al., 1995). If this composite structure is correct, then mechanisms usually proposed for cold slabs (e.g., transformational faulting on a MOW) could be viable in the Nazca slab despite its nominally low thermal parameter.

Since 2014, several broadband stations have been installed in the Amazon region of Brazil as part of the national Brazilian Seismographic Network (RSBR) (Bianchi et al., 2018). The coverage provided by these stations (Figure 1a), together with that provided by other national and international networks, offers a unique opportunity to closely investigate DFEs in the Peru-Brazil region. Luckily, RSBR stations were installed right before an unusual year of rather intense seismic activity (2015), which comprised a rare doublet and a relatively large number of aftershocks. In this work, we determine focal mechanisms and centroid depths for 28 DFEs along the Peru-Brazil border (Figure 1b), with the aim to investigate the stress conditions under which DFEs take place and, consequently, obtain insights into the physical mechanisms that trigger them. We found that DFEs in this region

occur within a narrow depth-range (587–659 km) and under a predominant down-dip compression (DDC) regime, consistent with nucleation inside a relatively narrow MOW at the bottom of the subducting slab. Moreover, most fault planes are found to be at  $\sim 45^\circ$  from a near-vertical direction of maximum compression, as expected from nucleation through superplastically filled anti-cracks in transformational faulting (Warren et al., 2007). Also, although nodal planes are found to be striking preferentially in the N-S direction, some fault planes deviate from this preferred orientation. These are typically events in the lower magnitude range that occurred shortly after a larger magnitude event, which might have locally affected horizontal stresses within the slab. Finally, we speculate that a composite thermal structure might be present in other flat-slab segments along the South American subduction front, as they display gaps in the distribution of deep earthquakes analogous to the one observed in the Nazca slab.

## 2. The 2014–2022 Deep-Focus Earthquake Sequence

Since the deployment of RSBR broadband stations in the Amazon region of Brazil in 2014, a total of 42 DFEs have been reported in the region by the USGS (Figure 1b), with magnitudes and depths ranging from 4.0 mb to 7.6 Mw and 515–655 km, respectively (see Table S1 in Supporting Information S1 for catalog information). Tables S1–S4 and Figures S1–S40 are located in Supporting Information S1. A total of 25 of these events occurred only in 2015, just a year following the installation of the first RSBR stations (Figures S39a and S39b in Supporting Information S1). Most of these 25 events occurred by the end of November and included an earthquake doublet consisting of two Mw 7.6 events separated  $\sim 5$  min apart and  $\sim 50$  km from each other. The doublet occurred on November 24th, it was preceded by a single 4.3 mb foreshock and was followed by nearly 20 aftershocks with magnitudes ranging from 4.0 mb to 6.7 Mw (Figures S39c and S39d in Supporting Information S1) (Ruiz et al., 2017; Ye et al., 2016). Up to 16 of these aftershocks took place within a time span of 1 week and followed shortly after the Mw 7.6 mainshocks (Jiménez et al., 2021; Ye et al., 2016; Zahradník et al., 2017).

Other large events within the 2014–2022 sequence had magnitudes in the  $5.9 \leq M_w \leq 7.1$  range. Those included events 32, 34, 38, and 41 (Table S1 in Supporting Information S1), each followed by at least one small (mb < 5) aftershock (events 33, 35, 39, and 42, respectively). These aftershocks occurred from nearly an hour to a few months after their corresponding mainshocks. Only event 30, with Mw 6.4, showed no aftershocks—within the USGS catalog threshold (4 mb)—despite its relatively large magnitude. Temporally and spatially clustered deep events are relatively common along the South American subduction zone (Okal & Bina, 1994; Ruiz et al., 2017; Ye et al., 2016). A low productivity of aftershocks is a common characteristic of warm slabs (Tibi et al., 2003), so the large number of aftershocks after the November 24th doublet is most unusual.

Studies on the source mechanism of DFEs in this region generally focused on the 2015 great doublet. Those studies revealed two consistent normal fault mechanisms with negligible non-double-couple (NDC) components and intermediate stresses aligned with the approximately N-S regional trend of deep-focus epicenters (Jiménez et al., 2021; Ye et al., 2016; Zahradník et al., 2017). They also indicated that both ruptures probably occurred along the same west-dipping fault plane ( $160^\circ$  strike and  $60^\circ$  dip, parallel to inferred slab strike), but in a segmented manner, with the first event rupturing towards SE and the second one rupturing towards NW (Ruiz et al., 2017; Ye et al., 2016; Zahradník et al., 2017). Aftershock distribution was observed to follow the regional N-S trend but failed to constrain the actual fault plane (Ruiz et al., 2017). Ye et al. (2016) suggested that the second event of the doublet was probably dynamically triggered by the S-wave from the first event, while Zahradník et al. (2017) proposed that the second event was triggered by static stress changes resulting from the first event. Jiménez et al. (2021), on the other hand, suggested that both events constituted mainshocks. Regarding their rupture processes, Ye et al. (2016) first suggested diversity of rupture, in which the second event would have been more dissipative than the first one and possibly nucleated under different conditions. This was in contrast to the findings of Ruiz et al. (2017), who reported similar rupture parameters for both events.

Apart from the great doublet, a total of 8 events ( $5.2 \leq M_w \leq 7.1$ ) of this sequence have focal mechanisms available in either the USGS or GCMT catalogs (see events 1, 19, 30, 32, 34, 35, 38, and 41, in Table S3 of the Supporting Information S1). It is worth noting that they all exhibit a radiation pattern remarkably similar to that obtained for the 2015 doublet. Furthermore, this observation is generally consistent with GCMT solutions available for events in the Peru-Brazil region that occurred since 1977 (Figure 1a). This suggests a quite uniform ambient stress regime for the triggering of these events, characterized by a predominant down-dip P-axes, along-strike B-axes and slab-normal T-axes (Kirby et al., 1995).

### 3. Data Selection, Data Processing, and Green's Functions

We collected seismograms from several broadband stations belonging to various networks operating in the continent ( $\Delta \leq 45^\circ$ ): the Brazilian Seismic Network (RSBR), which provided upper-hemisphere coverage for the deep events, especially through stations in the Amazonian region (see black squares in Figure 1a); other national (e.g., Colombia, Chile and Ecuador) and international (GSN, GEOFON, and GEOSCOPE) permanent networks, for which data were openly available through the EarthScope Consortium Wilber 3 (<https://ds.iris.edu/wilber3/>); and, finally, temporary stations deployed under the 3-basins Project (Assumpção et al., 2016; Chagas de Melo et al., 2018), which included stations in Uruguay, Argentina, Paraguay, Bolivia and Brazil. We did not include stations outside the South American continent to avoid using waveforms traveling through complex tectonic settings (e.g., the Caribbean) which could potentially introduce artifacts in our inversions. Our data selection thus contemplated local ( $\Delta \leq 5^\circ$ ), regional ( $5^\circ < \Delta < 30^\circ$ ) and teleseismic ( $\Delta \geq 30^\circ$ ) waveforms recorded within South America. Those data provided sufficient azimuthal coverage to tightly constrain the radiation pattern of the DFEs.

Theoretical arrival times were obtained for the main phases (P, S, sP, and pP) using the TauP utility (Crotwell et al., 1999) and the reference velocity model ak135 (Kennett et al., 1995). Seismograms were then cut within time windows starting at 70 s before the P-wave arrival and lengths that included the direct P and S phases as well as the pP and sP depth phases. More accurate first arrivals were visually picked after simulating the WWSSN short-period response on the vertical seismogram. The mean and trend were next removed, and a 5% cosine taper was applied before removal of the instrument response. The resulting displacement waveforms were then rotated into the great-circle-path, to naturally separate P and SV energy from SH energy. Seismograms were all decimated to 10 samples per second (s.p.s.) after applying an anti-aliasing filter. We carefully checked our data for errors in the reported instrument responses and/or component orientations and removed those for which metadata was found inaccurate.

For the computation of Green's functions, we used the wavenumber-integration method of Bouchon (1981), as implemented in the Computer Programs in Seismology (CPS) package of Herrmann (2013). We considered epicenters from the USGS catalog and, aiming at improving on the source-depth estimates for each event, we computed synthetics for a range of focal depths around the nominal values given in the catalog, at 10 km intervals (Table S1 in Supporting Information S1). The synthetic waveforms were obtained considering an impulsive source and the AK135-F reference Earth model, which consists of the AK135 velocity model of Kennett et al. (1995) with density and attenuation (Q) estimates added from free-oscillation data in Montagner and Kennett (1996). The model's sphericity was accounted for using an Earth-flattening transformation included in the CPS package (Herrmann, 2013). Synthetics started 70 s before the P-wave, with a sampling interval of either 0.5 or 0.2 s, depending on the frequency range considered for inversion (0.02–0.05 or 0.3–1.0 Hz, respectively), as explained later in the Methodology section. When using a sampling interval of 0.5 s, the total length of the synthetics was set to either 512 ( $\Delta < 900$  km) or 1,024 ( $\Delta \geq 900$  km) points; on the other hand, when using a sampling interval of 0.2 s, the total length was set to 1,024 ( $\Delta < 900$  km) or 2,048 ( $\Delta \geq 900$  km) points. These parameters allowed us to produce synthetic waveforms with sufficiently long time windows to include both P and S waves and the corresponding depth phases. The theoretical arrivals in the synthetic waveforms were determined using TauP (Crotwell et al., 1999).

### 4. Waveform Modeling Details

For the determination of the earthquake source mechanisms, we used the Cut-and-Paste (CAP) approach of Zhao and Helmberger (1994) and Zhu and Helmberger (1996). The CAP method assumes a pure double-couple (DC) source mechanism and performs a grid-search over the fault-parameter space (strike, dip, and rake) that yields the best fault orientation and slip direction for a given earthquake. We regard this assumption as valid for deep earthquakes because it is now accepted that no significant isotropic component is to be expected (Kawakatsu, 1991), and any significant NDC contributions are likely to result from either multiple faulting events (Frohlich, 1994; Houston, 2015) or from shear faulting in a highly anisotropic medium (J. Li et al., 2018). The CAP approach models the body-wave (P and S) segments independently and uses time shifts determined through waveform cross-correlation to align observations and predictions (Chang et al., 2019). These time shifts represent an efficient manner to account for inaccuracies in origin time, location, and model velocities during computation of the Green's functions (Zhao & Helmberger, 1994; Zhu & Helmberger, 1996).

**Table 1**  
*Description of the Cutting Scheme Employed in This Work to Obtain the Body-Wave Segments to Be Modeled*

Frequency range	Distance range <sup>a</sup>	Phase	Windows cut description <sup>b</sup>
0.02–0.05 Hz	Local	P	[tP – 55 s]–[tP + (tS – tP)/2]
		S	[tS – (tS – tP)/2]–[tS + 100 s]
	Regional	P	[tP – 55 s]–[tP + (tsP – tP)/2]
		S	[tS – (tS – tP)/2]–[tS + 100 s]
	Teleseismic	P	[tP – 55 s]–[tP + (tS – tsP)/2]
		S	[tS – (tS – tsP)/2]–[tS + 100 s]
0.3–1.0 Hz	Local	P	[tP – (tS – tP)/8]–[tP + (tS – tP)/8]
		S	[tS – (tS – tP)/8]–[tS + (tS – tP)/8]
	Regional	P	[tP – (tsP – tP)/8]–[tP + (tsP – tP)/8]
		S	[tS – (tS – tP)/8]–[tS + (tS – tP)/8]

<sup>a</sup>Local stations are those at  $\Delta \leq 5^\circ$ , regional are those within  $5^\circ < \Delta < 30^\circ$ , and teleseismic those at  $\Delta \geq 30^\circ$ . <sup>b</sup>The windows were cut based on the arrival times of P, S, and sP, identified as tP, tS, and tsP, respectively.

To perform the inversions, we initially aligned observed waveforms and Green's functions by cutting both from 55 s before the P-wave arrival to 100 s after the S-wave arrival. We then applied a zero-phase Butterworth band-pass filter with corner frequencies of 0.02 and 0.05 Hz (e.g., Zahradník et al., 2017) and decimated the observed seismograms to 2 s.p.s. This frequency range was selected after extensive testing aimed at determining the lowest possible frequency content with a signal-to-noise ratio (SNR) high-enough to model body waves. For the smallest events ( $m_b < 5$ ), we had to use a relatively higher frequency range between 0.3 and 1.0 Hz, and a sampling rate of 5 s.p.s. to obtain waveforms with a SNR suitable for waveform modeling. The use of this higher frequency range for small-magnitude events was critical because, as shown in the next section, it allowed us to determine focal mechanisms for 14 events for which there were no previously published solutions (events 6, 10–13, 17–18, 29, 31, 33, 37, 39–40, and 42, in Table 1 and Table S1 in Supporting Information S1).

Next, following the CAP approach, we split the filtered seismograms and their respective Green's functions into separate body-wave segments to be modeled individually. We extracted the P- and SV-wave segments from the radial (Pr and SVr) and vertical (Pz and SVz) components, while the SH segment was extracted from the transverse component, resulting in up to five traces to be modeled for a given station (Chang et al., 2019; Zhan & Kanamori, 2016).

Modeling time windows were set according to epicentral distance and frequency range for P and S, as described in Table 1. The windows were based on the main arrival times on the seismograms (P, S, and sP), and were defined to include the target phase while avoiding unwanted phases. Naturally, we used narrower windows in the higher frequency range when compared to the lower frequency range. For teleseismic stations ( $\Delta \geq 30^\circ$ ), we ensured that the depth phases (sP and pP) were included in the P-wave window to be modeled. This was done to improve event depth estimation during inversion, as the temporal separation between P, sP, and pP is known to strongly constrain source depth (e.g., Chu et al., 2009; Heyburn et al., 2013). Note that we did not consider teleseismic body wave windows in the higher frequency range (0.3–1.0 Hz) because they were not suitable for inversion due to very low SNRs. Similarly, we disregarded regional SV segments due to complications related to sP phase propagation.

Only windows with SNR above a given threshold were used in our inversions. The thresholds were determined experimentally according to the magnitude of the event regardless of segment type:  $\text{SNR} \geq 5$  for  $4.0 \leq M < 5.0$ ;  $\text{SNR} \geq 10$  for  $5.0 \leq M < 6.0$ ; and  $\text{SNR} \geq 15$  for  $6.0 \leq M < 7.0$ . For the largest events ( $7.0 \leq M_w \leq 7.6$ ), however, we were able to use thresholds of  $\text{SNR} \geq 20$  and  $\text{SNR} \geq 30$ , for P and S windows, respectively, due to the relatively larger amount of data available for inversion. Realize that the use of lower thresholds for the smaller events was expected, as SNR decreases with earthquake size.

The grid-search to determine the focal mechanism was carried out by varying each fault angle by  $10^\circ$  and computing the average misfit between predicted and observed seismograms for all possible fault orientations and slip directions. The solution with the least average misfit was selected as the best focal mechanism for the target earthquake. The scalar seismic moment was then obtained from the average scale factor between observed and

predicted seismograms for all components, and the moment magnitude was determined following the relationship given in Hanks and Kanamori (1979). Waveform misfits were assessed using the L2-norm of the difference between observations and predictions after normalizing by the number of data points, which ensured that different time windows contributed equally to the average misfit.

Recall that the CAP method allows for empirical time shifts between synthetic and observed waveforms before computation of the RMS misfit. This procedure is very efficient to overcome misalignment between observations and predictions resulting from imprecise velocity models and/or inaccuracies in event location (Leite Neto & Julià, 2023). These time shifts are determined from waveform cross-correlation and can lead to either an advance or a delay in the synthetics with respect to the observed seismograms. After considerable testing, we defined a correlation window length of 75% of the observed waveform window and constrained the time shifts to  $\pm 25$  or  $\pm 2$  s, depending on whether the frequency range was 0.02–0.05 or 0.3–1.0 Hz, respectively. Note that such discrepancy between the time tolerances is merely empirical, as we observed that small time shifts were required to align waveforms in the higher frequency range. We also avoided employing unnecessarily large tolerances since it might result in phase skipping during the inversions.

## 5. Results

All focal mechanisms, described by the three fault angles: strike (S), dip (D) and rake (R), and their preferred centroid depths (CD) determined in this study are summarized in Table 2. To illustrate our inversion results, we first describe the modeling for the 2015 deep-focus doublet (events 8 and 9, in Table 2), which represent the largest and most studied DFEs within the 2014–2022 sequence. After that, we briefly describe our results for the rest of the sequence. To facilitate comparison with previous studies, focal mechanisms are classified in Table 2 according to the Focal Mechanism Classification (FMC) criterion of Álvarez-Gómez (2019), which conducts a double-couple (DC) classification based on the orientation of the P, T, and B axes.

### 5.1. The Great 2015 Deep-Focus Doublet

For the first event of the doublet (event 8), we inverted a total of 332 waveform segments from 132 stations in the 0.02–0.05 Hz frequency range (Figure 2 and Figure S4 in Supporting Information S1). We obtained a normal fault solution ( $350^\circ \pm 0^\circ$ ,  $40^\circ \pm 0^\circ$ ,  $-80^\circ \pm 0^\circ$ ) and a preferred centroid depth of  $616 \pm 10$  km, with a scalar seismic moment of  $1.81 \pm 0.02e + 27$  dyne-cm, which corresponds to a moment magnitude of Mw 7.5 (Table 2 and Figure 2a). This solution showed remarkable stability within the entire range of investigated source depths (Figure 2b and Figure S4b in Supporting Information S1). Also, most of the synthetic waveforms produced with this solution were in excellent agreement with the observed traces. This excellent match includes stations at teleseismic distances, for which we included depth phases in the P-wave segments (see some examples in Figure 2c and all matches in Figure S4c of the Supporting Information S1). For this event, we excluded teleseismic SV waveforms due to its contamination with the P-wave from event 9 at those distances. However, we still managed to use S-wave segments taken from the teleseismic transverse recordings (SH), since events 8 and 9 have virtually the same location (only ~50 km apart) and consequently little P-wave energy was leaked onto the transverse (SH) components after rotation. The uncertainties in this work were all assessed through jackknife resampling (Miller, 1974; Quenouille, 1949, 1956), after removing one station at a time.

For the second event (event 9), we obtained a very similar normal fault solution ( $350^\circ \pm 0^\circ$ ,  $30^\circ \pm 0^\circ$ ,  $-90^\circ \pm 0^\circ$ ), centroid depth ( $621 \pm 13$  km), and scalar seismic moment ( $1.93 \pm 0.02e + 27$  dyne-cm), again corresponding to a magnitude of Mw 7.5. Those results were achieved using the same frequency range (Table 2 and Figure 2d) as for the previous event. This solution was again remarkably stable within the studied depth range and produced excellent synthetic waveform matches with most of the 88 observed waveforms (Figure 2 and Figure S5 in Supporting Information S1). Note that, for this event, we had to use less waveforms in our inversion when compared to event 8. First, P-wave recordings were often contaminated with signal-generated noise from the first event, which led to a considerable reduction of the SNRs for regional P-wave segments. Second, as explained before, the contamination of the P-wave from this event with the S-wave from event 8 at teleseismic distances rendered teleseismic P-wave segments unusable. Additionally, this contamination prevented us from including depth phases in our analysis; despite that, the preferred centroid depth of 621 km was well defined in the misfit curve (Figure 2e and Figure S5b in Supporting Information S1). We note, nonetheless, that a second minimum occurs in the misfit curve at 661 km depth, which is probably caused by the abrupt change in velocity at ~660 km.

**Table 2**  
*Earthquake Focal Mechanisms Determined in This Study for a Total of 28 DFEs From the 2014 to 2022 Sequence*

Event	S (°)	D (°)	R (°)	CD (km)	M <sub>0</sub> (dyne-cm)	Mw	Type	Quality	FR (Hz)
1	180 ± 8	50 ± 7	-80 ± 11	571 ± 18	7.36 ± 1.06e + 23	5.2 ± 0.04	N	A	0.02–0.05
3	20 ± 4	30 ± 0 <sup>a</sup>	-80 ± 4	557 <sup>b</sup> ± 9	1.36 ± 0.02e + 24	5.4 ± 0.004	N	A	0.02–0.05
6	190 ± 8	60 ± 10	-10 ± 6	584 ± 13	3.28 ± 0.77e + 23	5.0 ± 0.07	SS-N	B	0.3–1.0
8	350 ± 0	40 ± 0	-80 ± 0	616 <sup>b</sup> ± 10	1.81 ± 0.02e + 27	7.5 ± 0.003	N	A	0.02–0.05
9	350 ± 0	30 ± 0	-90 ± 0	621 ± 13	1.93 ± 0.02e + 27	7.5 ± 0.003	N	A	0.02–0.05
10	110 ± 20	50 ± 9	-80 ± 8	595 <sup>c</sup>	1.63 ± 0.34e + 23	4.8 ± 0.05	N	B	0.3–1.0
11	310 ± 64	70 ± 35	-60 ± 28	629 ± 17	9.61 ± 0.76e + 22	4.6 ± 0.03	N-SS	B	0.3–1.0
12	150 ± 32	50 ± 18	-60 ± 35	587 ± 8	1.82 ± 0.27e + 23	4.8 ± 0.04	N-SS	B	0.3–1.0
13	250 ± 145	20 ± 0	-20 ± 67	590 <sup>c</sup>	2.27 ± 4.57e + 22	4.2 ± 0.22	N	D	0.3–1.0
14	170 ± 4	40 ± 0	-70 ± 0	659 ± 4	3.66 ± 0.11e + 23	5.0 ± 0.01	N	B	0.02–0.05
17	200 ± 41	40 ± 5	-90 ± 24	655 <sup>c</sup>	1.25 ± 0.67e + 23	4.7 ± 0.11	N	B	0.3–1.0
18	300 ± 111	70 ± 11	-80 ± 15	592 <sup>c</sup>	4.60 ± 2.17e + 22	4.4 ± 0.11	N	B	0.3–1.0
19	350 ± 0	30 ± 0	-90 ± 0	603 <sup>b</sup> ± 9	1.27 ± 0.01e + 26	6.7 ± 0.002	N	A	0.02–0.05
22	350 ± 0	60 ± 0	-80 ± 0	636 ± 15	2.75 ± 0.03e + 23	4.9 ± 0.003	N	A	0.02–0.05
24	170 ± 2	50 ± 2	-90 ± 3	617 ± 13	5.44 ± 0.19e + 23	5.1 ± 0.01	N	A	0.02–0.05
29	230 ± 131	20 ± 23	-40 ± 15	643 ± 8	1.24 ± 0.78e + 23	4.7 ± 0.17	N	B	0.3–1.0
30	350 ± 0	20 ± 0	-80 ± 0	642 <sup>b</sup> ± 19	4.72 ± 0.01e + 25	6.4 ± 0.001	N	A	0.02–0.05
31	90 ± 35	70 ± 19	-90 ± 59	590 <sup>c</sup>	7.79 ± 2.94e + 22	4.6 ± 0.08	N	B	0.3–1.0
32	340 ± 1	40 ± 1	-90 ± 1	620 <sup>b</sup> ± 14	4.83 ± 0.02e + 26	7.1 ± 0.001	N	A	0.02–0.05
33	60 ± 26	30 ± 8	-50 ± 9	626 ± 8	2.58 ± 0.55e + 23	4.9 ± 0.06	N	C	0.3–1.0
34	350 ± 1	40 ± 0	-80 ± 2	570 <sup>b</sup> ± 12	1.64 ± 0.02e + 26	6.8 ± 0.003	N	A	0.02–0.05
35	10 ± 4	20 ± 0	-80 ± 3	564 ± 5	4.76 ± 0.22e + 23	5.1 ± 0.01	N	A	0.02–0.05
37	180 ± 66	20 ± 30	-70 ± 42	557 <sup>c</sup>	5.59 ± 6.04e + 22	4.5 ± 0.17	N	B	0.3–1.0
38	350 ± 0	40 ± 0	-80 ± 0	599 <sup>b</sup> ± 18	9.31 ± 0.12e + 24	5.9 ± 0.004	N	A	0.02–0.05
39	220 ± 21	40 ± 28	-30 ± 7	605 ± 5	7.26 ± 3.24e + 22	4.5 ± 0.10	N-SS	B	0.3–1.0
40	280 ± 58	70 ± 30	-30 ± 24	580 <sup>c</sup>	1.70 ± 0.66e + 23	4.8 ± 0.13	SS-N	B	0.3–1.0
41	350 ± 0	20 ± 0	-80 ± 0	623 <sup>b</sup> ± 12	6.16 ± 0.08e + 25	6.5 ± 0.004	N	A	0.02–0.05
42	350 ± 69	80 ± 0	60 ± 56	605 <sup>c</sup>	7.80 ± 0.65e + 23	5.2 ± 0.02	R-SS	B	0.3–1.0

<sup>a</sup>An error of 0° means that uncertainties are estimated to be within the grid-search steps (10°), that is, that fault angles did not change after removal of one station. <sup>b</sup>The centroid depth was determined with the inclusion of depth phases in the inversion. <sup>c</sup>The centroid depth was fixed to be the hypocenter depth given by the USGS catalog. In these cases, there was no clear minimum in the misfit curve and thus we could not select a preferred depth.

The focal mechanisms obtained in this study for the earthquake doublet are consistent with those determined in independent works using a variety of approaches and data sets (Jiménez et al., 2021; Ye et al., 2016; Zahradník et al., 2017), and with solutions reported in the USGS and GCMT catalogs (see Table S2 in Supporting Information S1 for comparison). Overall, we observed that our results are in closer agreement to those in the GCMT catalog. Regarding centroid depths, our estimates generally agree with previous estimates (Table S2 in Supporting Information S1). Centroid depths in Jiménez et al. (2021), however, were considerably deeper, suggesting that both events happened around the base of the mantle transition zone (~660 km). Our depth estimates suggest centroids were just ~5 km apart, closer than indicated in previous studies. We stress that we included depth phases in our inversion for event 8, which were satisfactorily modeled (see some examples in Figure 2c), thus ensuring accurate depth estimates. Finally, regarding seismic moments, we observed that our estimates for events 8 and 9 are very similar, around Mw 7.5 (Table 2 and Table S2 in Supporting Information S1), suggesting similar sizes. Compared to previous estimates, we obtained smaller moments for the doublet (Table S2 in Supporting Information S1).

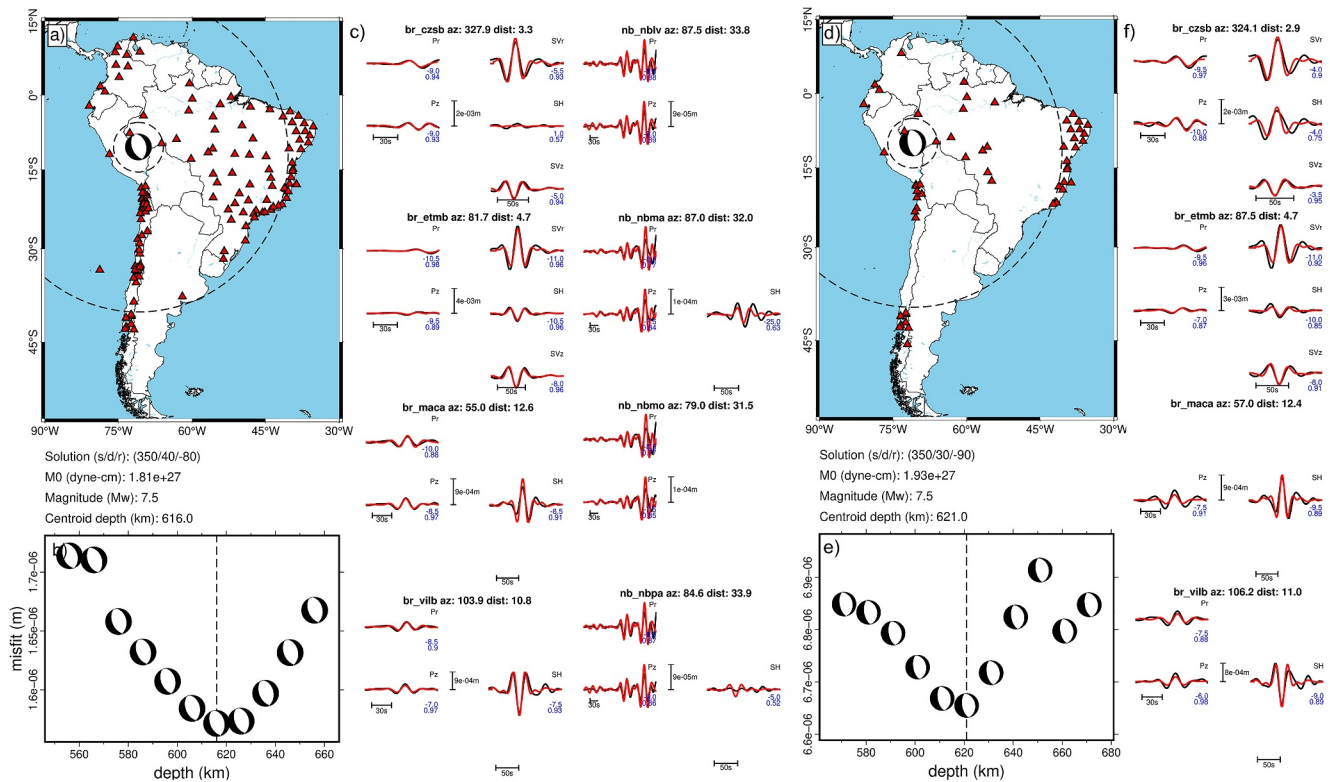


**Figure 2.** Examples of waveform fitting produced by the focal mechanisms determined for the 2015 deep-focus doublet, events 8 and 9; (a) map showing the preferred solution for event 8 and the distribution of stations that were used in the inversion. Dashed circles indicate radii of 5° and 30° from epicenter; (b) distribution of focal mechanisms with investigated centroid depths. The preferred solution, which is the one that produced the best fit to observations is indicated by the vertical dashed line; (c) examples of waveform matches produced by this preferred solution. Black and red waveforms denote observations and synthetics, respectively. Station names, azimuths and distances are shown above each station panel. Time shifts (top) and cross-correlation coefficients (bottom) are shown in blue at the lower right corner of each panel. Wave segments (Pr, Pz, SVr, SH, and SVz) are identified at the upper right corners; (d–f) the same as in (a)–(c) but for event 9. For the complete waveform matches, see Figures S4 and S5 in Supporting Information S1.

In summary, our results suggest that the 2015 deep-focus doublet was composed of two events with very similar ruptures, in terms of focal mechanism, centroid depth, and size. This observation substantiates previous claims that both events ruptured along the same fault plane (e.g., Zahradník et al., 2017).

## 5.2. The 2014–2022 Deep-Focus Sequence

Regarding the whole seismic sequence, we were able to determine focal mechanisms and centroid depths for 28 of the 42 DFEs listed in Table S1 of the Supporting Information S1 (see Figure 3). In general, our inversions with the CAP approach led to robust solutions that provided reasonable fits to observed seismograms (Figures S1–S28 in Supporting Information S1). These events span a relatively wide magnitude range, from Mw 4.2 to Mw 7.5 (Table 2). In the following, we briefly describe our inversions and compare our focal mechanisms and centroid depths with independent assessments when available.

### 5.2.1. Goodness of Fit

As explained before, inversions were performed at either the 0.02–0.05 Hz frequency range or the 0.3–1.0 Hz frequency range (Table 2), depending on magnitude. In general, we observed good waveform matches at either frequency range (see Figures S1–S28 in Supporting Information S1), as illustrated through waveform fits for events 14 (Figure 4f) and 12 (Figure 4c), respectively. Note that both events utilized the same number of stations (5) at both local and regional distances, and that both were aftershocks of the 2015 doublet (Table S1 in Supporting Information S1). It is worth mentioning that the use of a higher frequency range for smaller-magnitude events was critical, as it allowed us to determine focal mechanisms for (smaller) events that showed poor SNRs in the 0.02–0.05 Hz frequency range.

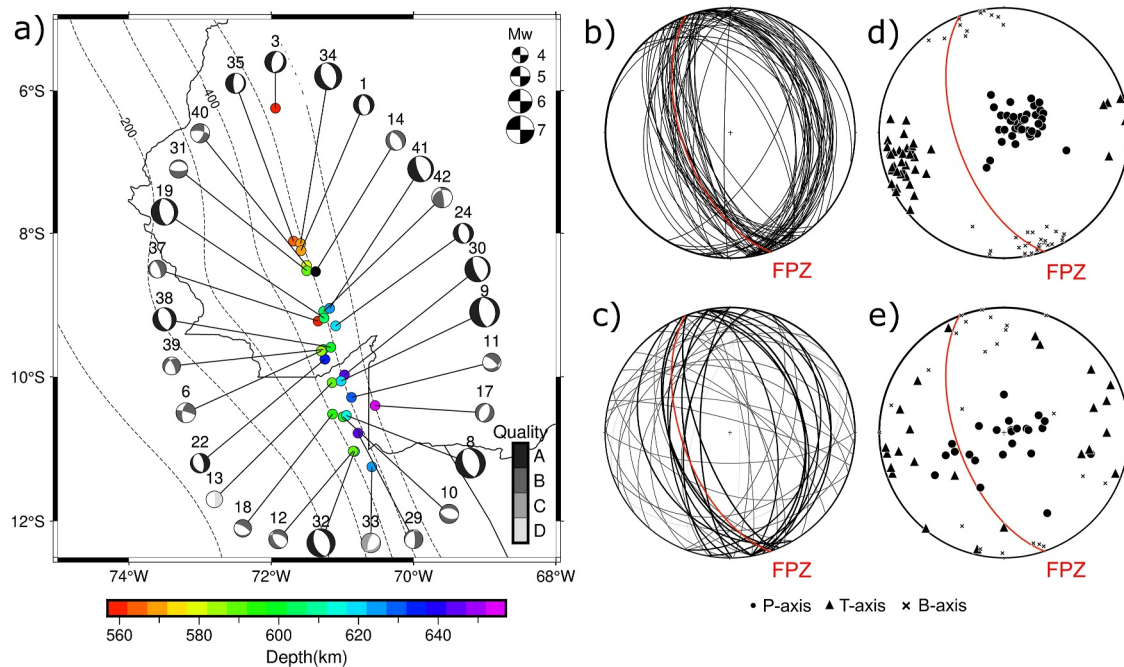


**Figure 3.** Focal mechanisms determined for 28 events in the 2014–2022 deep-focus sequence. (a) Distribution of the obtained focal solutions sized by magnitude and colored in grayscale by quality (A, B, C and D) (Table 2). Each solution in the map is identified by event number in Tables S1 and S2 in Supporting Information S1. The epicenters are colored by centroid depths. Dashed lines delineate the Nazca slab depth from Slab 2 (Hayes et al., 2018); (b) nodal planes from 39 GCMT focal mechanisms in the Peru-Brazil region occurred between 1977 and 2022 and  $5.1 \leq M_w \leq 7.6$  (Figure 1a) plotted on a stereonet using FaultKin (Allmendinger et al., 2012; Marrett & Allmendinger, 1990). The fault zone orientation, striking  $160^\circ$  and dipping  $60^\circ$ , as proposed by Zahradnik et al. (2017) is shown in red (FPZ); (c) nodal planes from the solutions obtained in this study. Planes are colored in grayscale according to quality, as in (a); (d) Principal axes (P, T, and B) from the GCMT solutions and (e) principal axes from this study. Another version of this figure with focal mechanisms colored by faulting style can be found in Figure S30 of the Supporting Information S1.

Although our inversions in the lower frequency range were quite straightforward, the inversions in the higher frequency range were found to be more challenging. The most important challenge was presented by the contamination of P- and S-wave segments at regional distances, which resulted in waveform complications. This contamination was verified through computation of travel-times, revealing up-going and down-going direct phases at similar times or multiple P or S reflections present in the recordings. As these waveforms were difficult to model, we simply removed them from inversion. At lower frequencies, on the other hand, this contamination appeared to be less critical, as we did not observe any difficulties in matching synthetic and observed waveforms.

A second challenge arose from the use of an inaccurate attenuation model. We noticed that our attenuation model was perhaps too severe on the higher frequency range, as it made amplitudes decay faster than actually required. This severity can be noticed in some waveform fits as discrete, unmodelled high-frequency features in the observed waveforms (see e.g., Figures S16 and S25 in Supporting Information S1). This observation suggests that the attenuation model in AK135-F might have to be tailored to our study region in order to improve waveform fits in the higher frequency range. In any case, as demonstrated through Figures S1–S28 in Supporting Information S1, our solutions display acceptable waveform fits and are quite robust, showing little variation in focal mechanism within the investigated depth ranges.

### 5.2.2. Focal Mechanisms

From the 28 focal mechanisms determined in this study, 22 of them describe pure normal faulting, while the other 6 mechanisms describe different types of oblique faulting: 3 normal with strike-slip component, 2 strike-slip with normal component, and 1 reverse with strike-slip component (see Figure 5a and Table 2).

Only 10 out of the 28 inverted events in Table 2 have source mechanisms available in either the USGS or the GCMT catalogs. Generally, these catalogs provide focal solutions for events with magnitudes greater than  $M_w \sim 5.0$ . Comparing the available solutions with ours, we observed that the agreement is excellent (see Table S3

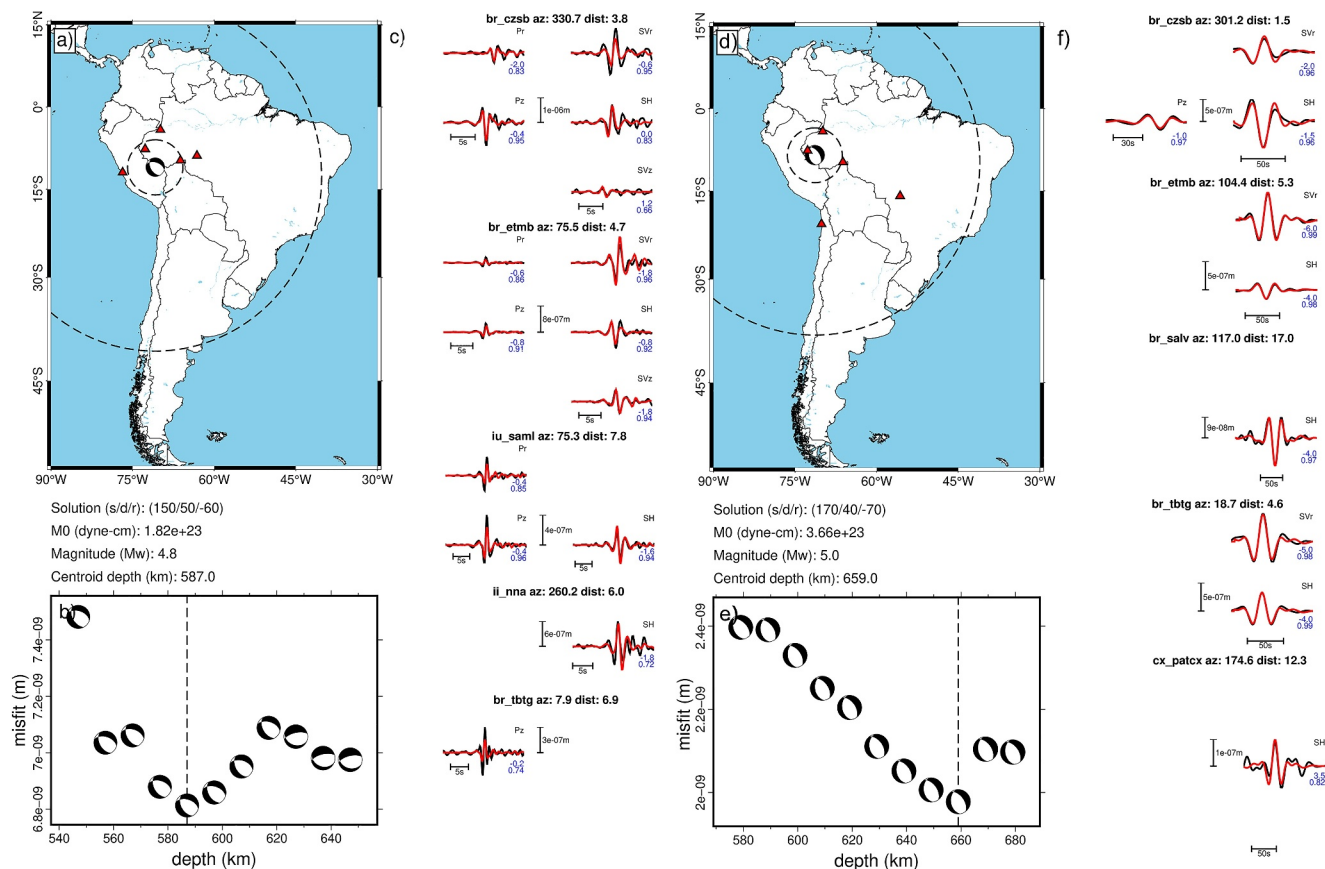


**Figure 4.** Examples of waveform inversions for the two frequency ranges used in this study, 0.02–0.05 Hz (event 12, from a to c), and 0.3–1.0 Hz (event 14, from d to f). Features in this figure are the same described in Figure 2.

in Supporting Information S1). The only strong disagreement was perhaps found for the fault strike of event 1, which deviates about  $\sim 35^\circ$  from that reported in the GCMT catalog, but the fault type remained roughly the same. This difference might be due to the few traces available (14 traces from 7 stations), since this event happened in the beginning of 2014 when RSBP stations in the Amazonian region were not yet installed (Table S4 and Figure S1 in Supporting Information S1). Also, compared with the GCMT orientation, our fault strike is in relatively better agreement with the observed N-S trend of the B-axes (see mechanism 1 in Figure 3a).

We now compare our results, which span from 2014 to 2022, with GCMT solutions within the extended period from 1977 to 2022 (Dziewonski et al., 1981; Ekström et al., 2012). According to the 39 moment tensors available in the GCMT catalog ( $5.1 \leq M_w \leq 7.6$ ) for this extended period, earthquake focal mechanisms along the Peru-Brazil border are usually normal, with only two cases of normal to strike-slip faulting (Figure 5b). Interestingly, there seems to be a slight dependency with depth in terms of faulting orientation for this set of solutions. Shallower events seem to show B-axis plunges deviating a little more from the horizontal than deeper events. In our set of solutions, in Figure 5a, we did not observe this trend, but our results also indicated the predominance of normal faults with a few normal with strike-slip faults. Contrary to GCMT solutions, we observe two strike-slip with normal component faults, events 6 and 40, and an oblique reverse fault, event 42 (Figure 5a). The robustness of these disparate focal mechanisms is investigated later in the manuscript (Section 6.1.2).

### 5.2.3. Seismic Moment

The values found for seismic moments ranged from  $2.27e + 22$  to  $1.93e + 27$  dyne-cm, corresponding to magnitudes from  $M_w 4.2$  to  $7.5$  (Table 2). Regarding these seismic moments, we obtain values between 3% and 92% smaller than those provided by the two catalogs ( $\sim 26\%$  smaller on average, see Table S3 in Supporting Information S1). Note that, in general, uncertainties in  $M_0$  are small and do not explain such discrepancies. For

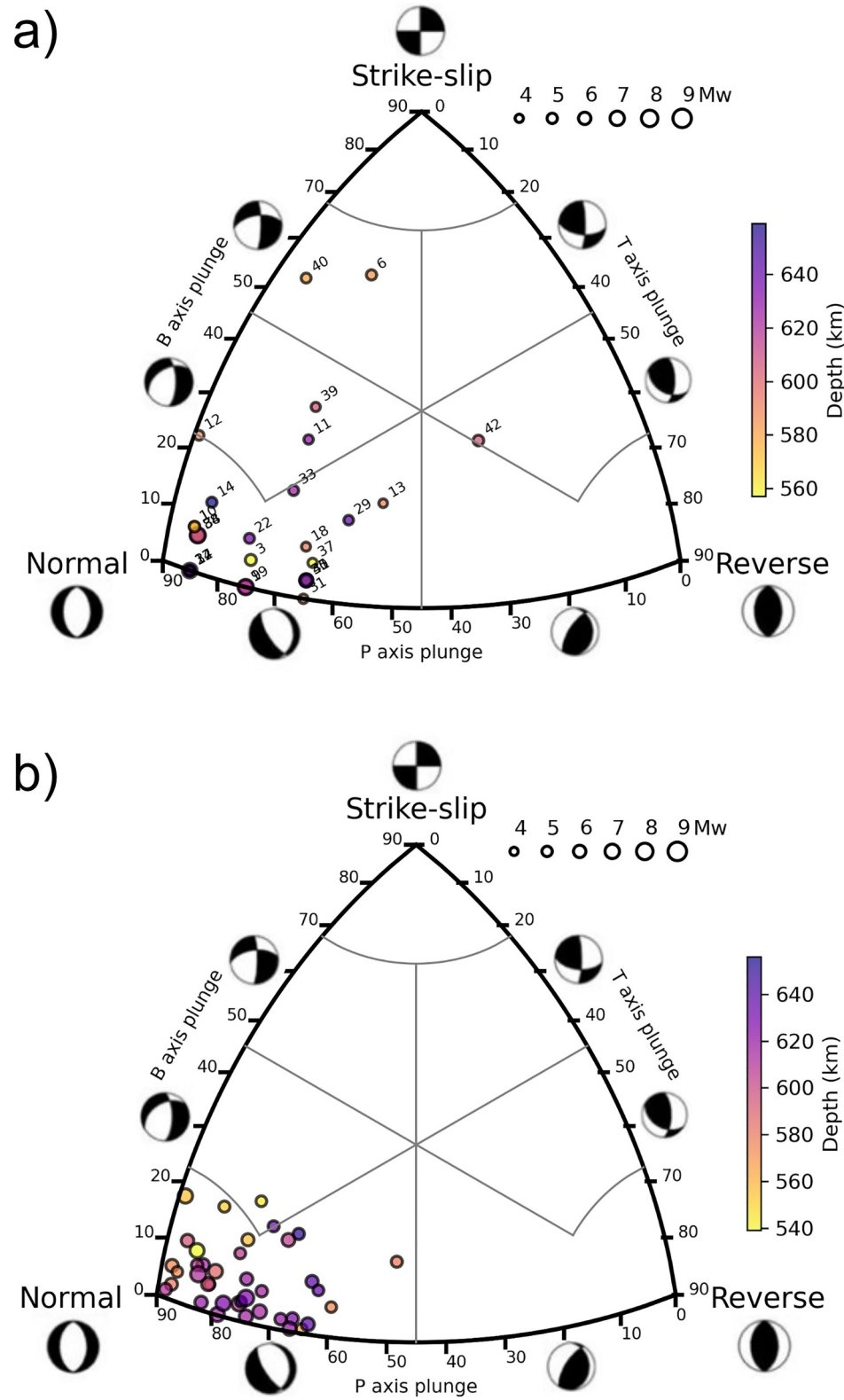


Figure 5.

event 19, a Mw 6.7, our  $M_0$  estimate ( $1.27 \pm 0.01e + 26$  dyne-cm) was remarkably close to those from USGS ( $1.21e + 26$  dyne-cm) and GCMT ( $1.34e + 26$  dyne-cm), being  $\sim 5\%$  larger and  $\sim 5\%$  smaller, respectively; for event 35, a Mw 5.1, on the other hand, our estimate ( $4.76 \pm 0.22e + 23$  dyne-cm) was very different from the previous estimate from GCMT ( $1.36e + 24$  dyne-cm, corresponding to Mw 5.4), being almost three times smaller. The only exception occurs for event 1 (Mw 5.2), for which uncertainties in  $M_0$  ( $7.36 \pm 1.06e + 23$  dyne-cm) can explain values from 9% to 46% smaller than the estimate given by the GCMT catalog ( $9.18e + 23$  dyne-cm).

We investigated whether such systematic smaller values were due to overestimation of Q values in the reference model, by systematically reducing Q in 10% steps until it reached 50% of its original values (Table S5 in Supporting Information S1). We applied the same reduction for both P and S attenuation. Our tests showed that overestimation in Q structure does not account for the systematically smaller seismic moments found in this study. Alternatively, it is possible that  $M_0$  is being underestimated in our study by the assumption of an impulsive source when modeling the lower frequency range (0.02–0.05 Hz). Recent studies on the 2023 Mw 7.8 and 7.5 Turkey earthquakes, for instance, considered triangular time functions (Čejka et al., 2023; Zahradník et al., 2023), and Zahradník et al. (2017) reported durations of 15 and 20 s for the 2015 earthquake doublet in our study. Most likely, the systematically smaller values result from a combination of an inaccurate attenuation model and an unaccounted source time function. Nevertheless, it is noteworthy that our inversions used considerably more data and a wider range of distances than other independent studies, providing solutions that showed good fit to local, regional and teleseismic observations.

#### 5.2.4. Centroid Depths

Centroid depths were determined by selecting the global minimum in the misfit curves. In the best cases, we observed well-behaved misfit curves with a single minimum, unambiguously indicating the optimal depth for the event (see e.g., Figures S1 and S13 in Supporting Information S1). In some other cases, the curves were a bit more challenging, with more than one minimum; but, as their shapes were relatively simple, we could also identify a global minimum with good accuracy and settle on a centroid depth (see e.g., Figures S5 and S20 in Supporting Information S1). Finally, in the worst-case scenario (events 10, 13, 17, 18, 31, 37, 40, and 42), the curve shape was found to be cumbersome, and we could not determine the preferred depth with any degree of confidence (see Figures S9 and S26 in Supporting Information S1 as examples). In such cases we fixed centroid depths to the USGS hypocentral depth and used the corresponding focal solution as our preferred mechanism (see Table 2).

An abrupt decrease in the rms misfit was observed around 660 km depth when that depth was included in the investigated depth range (see e.g., Figure S19 in Supporting Information S1). In Figure S15 of the Supporting Information S1, for instance, such a decrease almost became a global minimum. We sometimes observed abrupt increases in the rms around those depths as well (see Figure S10 in Supporting Information S1, as an example). Such features are probably artifacts due to the source being placed near the 660 km seismic discontinuity. Because deep events are not expected to occur below those depths, we disregarded such minima as physically unfeasible. In particular, for event 35 (Figure S22 in Supporting Information S1), we had to expand the investigated depth range up to 684 km to check if the observed decrease in rms from 614 to 634 km would lead towards a global minimum, which was not the case.

We stress that the inclusion of depth phases in our inversions was only possible for earthquakes with  $M_w \geq 5.4$ , which showed clear P, sP, and pP observations at teleseismic distances. Centroid depths estimated with the help of depth phases are indicated in Table 2. Overall, we observed centroid depths ranging from 557 to 659 km, defining a quite narrow ( $\sim 100$  km thick) zone of deep-focus seismicity. Note that events with fixed centroid depths are all within this estimated depth range (Table 2).

**Figure 5.** Focal mechanisms for DFEs in the Peru-Brazil border region classified according to the seismic moment tensor main axes plunges: (a) solutions from this study, 28 earthquakes with  $4.2 \leq M_w \leq 7.5$  from 2014 to 2022 and (b) solutions available in the GCMT catalog, 39 events with  $5.1 \leq M_w \leq 7.6$  from 1977 to 2022. The FMC program (Álvarez-Gómez, 2019) was used to classify the focal mechanisms and draw the diagrams, which are based on the Kaverina projection (Kaverina et al., 1996). The classification allows for up to seven styles of faulting: normal (N), normal with strike-slip (N-SS), strike-slip with normal (SS-N), strike-slip (SS), strike-slip with reverse (SS-R), reverse with strike-slip (R-SS) and reverse (R).

### 5.2.5. Qualitative Grading Scheme

Finally, prior to interpretation, we qualitatively graded our solutions according to fault mechanism robustness and depth resolution (Figure 3a). In our qualitative classification, we assigned qualities from A to D to our 28 solutions (Table 2). We attributed quality A to the more reliable solutions, in which both the mechanism and centroid depth are well determined. For example, for the 2015 doublet (events 8 and 9), we were able to easily determine their preferred depths and observed consistent mechanisms across the investigated depth range (Figures S4b and S5b in Supporting Information S1). Quality B was assigned to events for which faulting style was observed to be robust within the investigated depth range, but preferred depth was ambiguous due to an ill-defined minimum (see e.g., Figure S23b in Supporting Information S1). Quality C was attributed to solutions with non-robust mechanisms but well-resolved depths (Figure S20 in Supporting Information S1, event 33). Finally, quality D was given to those solutions with both unreliable mechanisms and inaccurate depths (Figure S9b in Supporting Information S1, event 13). Most of our solutions were qualified as either A or B (see Table 2). Notably, all solutions that included depth phases in the inversion were found to be of A quality; only two events, event 33 (C) and event 13 (D), did not qualify as A or B.

## 6. Discussion

### 6.1. Variability in Faulting Style

The predominant faulting style in our data set closely follows that of the 2015 doublet (Figures S6b–S9b in Supporting Information S1) and is consistent with the faulting style displayed by the CGMT solutions. The solutions indicate that normal-faulting (22 events out of 28), with a near vertical P-axis and near horizontal B- and T-axis (see Figures 3 and 5a and Figure S30a in Supporting Information S1) is predominant. We emphasize that, due to the coverage provided by our set of stations, we were able to determine focal mechanisms for events as small as Mw 4.2, so our set of solutions expand the range for which this faulting style is observed. For most of these normal-faulting solutions (17 events), B-axes orientations vary about the N-S direction, roughly following the strike of the linear distribution of DFEs in the region, while T-axes are oriented almost perpendicular to them (specifically events 1, 3, 8, 9, 13, 14, 17, 19, 22, 24, 30, 32, 34, 35, 37, 38, and 41) (Figures 3a and 3e). In fact, we noted that all events with Mw > 5.2 were pure normal faults, in reasonable agreement with the predominant configuration of the P, T, and B axes.

#### 6.1.1. Variability Within Normal Faulting

Some of our solutions in the lower-magnitude range display a normal faulting style that is rotated with respect to the predominant style around the compressional axis. Solutions 3 and 17 presented small deviations from the predominant B-axis orientation, with B-axes tending to move a bit towards NE. Note that such small deviations also occur within the GCMT solutions (Figure 3d). Event 17, however, has relatively high uncertainties in its fault angles that could explain such deviation; but event 3 is one of the best constrained solutions in our set (Table 2). Events 10, 18, 29, 31, and 33, on the other hand, display substantial deviations from the predominant B-axis orientation, suggesting a change from strike-parallel B-axis to strike-parallel T-axis (Figures 3a and 3b). Events 10, 18, 29, and 33 were clearly small aftershocks (Mw from 4.4 to 4.9) in our sequence, as events 10, 18, and 29 occurred shortly after the 2015 doublet, and event 33 followed event 32 (Mw 7.1); event 31, on the other hand, occurred more than a year after event 30 (Mw 6.4) and nearly 5 months before event 32 (Mw 7.1) (Table S1 in Supporting Information S1). Note that the mechanisms found for events 10, 18, and 31 are very similar (Figure 3a). Uncertainties for some of these events were very high (events 18 and 29), but uncertainties for events 10, 31, and 33 suggest that their mechanisms are reasonably stable. Note, however, that the solution found for event 33 was assigned a C quality, which means the focal mechanism is not robust.

To further investigate the robustness of events 10 and 31, we performed a constrained grid-search, so that strike, dip, and rake were restricted to vary from 330° to 30°, from 25° to 65° and from –90° to –40°, respectively, forcing the search for normal mechanisms consistent with the predominant pattern. For event 31, we observed that the unconstrained solution produced a better fit to observations (see Figure S35 in Supporting Information S1 and COHC, MCRA, CHSH, ANTS, VCES, PUYO in Figure S36c of the Supporting Information S1), suggesting that anomalous, orthogonal normal faulting might have occurred in the region. For event 10, the constrained mechanism provided a better amplitude fit to SAML, and correctly reproduced the observed P-wave polarity in ETMB (Figure S34 in Supporting Information S1); on the other hand, the unconstrained solution showed better amplitude

fit in NNA, but both solutions produced the correct polarity for this station (Figures S33c and S33f in Supporting Information S1). Thus, an overall normal faulting style consistent with the regional pattern, cannot be ruled out.

### 6.1.2. Deviations From Normal Faulting

Most interestingly, a few of our solutions present significant deviations from the predominant normal-faulting style. These events, all with  $M_w \leq 5.2$ , consist of six oblique faults, mainly normal with a small strike-slip component (events 11, 12, and 39), but also include strike-slip faults with a small normal component (events 6 and 40), and a single event showing reverse faulting with a small strike-slip component (event 42). The three normal with strike-slip faults (from  $M_w$  4.5 to 4.8) still display a near vertical P-axis but with variable B-axis orientations: approximately N-S for event 39, NW-SE for event 12, and E-W for event 11 (Figure 3a). Events 11 and 12 are aftershocks of the 2015 doublet and event 39 is an aftershock from a  $M_w$  5.9 (Table S1 in Supporting Information S1). Because two normal with strike-slip faults were also present among the 1977–2022 GCMT solutions in the Peru-Brazil segment (Figure 5b), we can conclude that such a pattern is plausible but unusual in this region. This pattern seems relatively more common in the Argentina-Bolivia segment (Figure S29a in Supporting Information S1).

The two strike-slip with normal component faults, events 6 and 40 ( $M_w$  5.0 and 4.8, respectively), on the other hand, show opposite slip directions but basically the same orientation of the nodal planes. Both preceded great ruptures in our sequence, the  $M_w$  7.5 doublet and event 41 ( $M_w$  6.5), respectively. It is noteworthy that there is no evidence of such faulting style in any deep-focus seismicity segment in South America within the reference catalog (Figure S29a in Supporting Information S1). The radiation pattern found for event 40 was observed to be poorly constrained, where uncertainties in rake can change its strike-slip with normal mechanism ( $280^\circ \pm 58^\circ$ ,  $70^\circ \pm 30^\circ$ ,  $-30^\circ \pm 24^\circ$ ) to either pure strike-slip or normal with strike-slip.

On the other hand, the small uncertainties in the fault angles of the oblique strike-slip mechanism obtained for event 6 suggests that it is a reliable observation ( $190^\circ \pm 8^\circ$ ,  $60^\circ \pm 10^\circ$ ,  $-10^\circ \pm 6^\circ$ ). As for event 10, we run a constrained inversion to verify the robustness of our solution. We observed that both solutions (constrained and unconstrained) produced very similar waveform matches, but our unconstrained solution was the one that provided the best fit for the P waveform of station TBTG (compare Figures S31c and S31f in Supporting Information S1). As shown in Figure S32 of the Supporting Information S1, TBTG is the only station that expects a substantial change in polarity between the two solutions (Figures S32a and S32b in Supporting Information S1) and is clear that the constrained solution does not provide the correct polarity for the P-wave at TBTG (Figure S32c in Supporting Information S1). Although this event preceded the 2015 doublet by nearly a month (Table S1 in Supporting Information S1), it is not clear to us how such unusual faulting could be explained.

Finally, the single case of reverse fault mechanism ( $M_w$  5.2 event 42 in Figure 3a) suggests a notable change to a near horizontal P-axis and a near vertical T-axis. The radiation pattern for this event was found to be unstable, since uncertainties in rake can explain from reverse to strike-slip faulting ( $350^\circ \pm 69^\circ$ ,  $80^\circ \pm 0^\circ$ ,  $60^\circ \pm 56^\circ$ ). Note that although this solution has relatively large uncertainties, there are some reverse faulting observations in other deep-focus segments in South America, in Bolivia and Argentina (see Figure S29a in Supporting Information S1). Thus, we ran a constrained inversion for this event and found that the reverse mechanism provides a better fit to observations (Figure S38 in Supporting Information S1).

Because most of the solutions that deviated from the normal faulting regime were small-magnitude aftershocks ( $M_w \leq 5.2$ ), we suggest that such deviations could be due to stress changes imposed by their respective mainshocks. Thus, our results indicate that oblique strike-slip, oblique reverse, and orthogonal normal faulting may also occur along the predominant normal style in the Peru-Brazil segment of deep-focus seismicity if the predominant stress field is perturbed. It is noteworthy that event 6, the oblique strike-slip mechanism, does not seem to be an aftershock from any event within our sequence (Table S1 in Supporting Information S1), and thus it is not clear to us how the ambient stresses changed before event nucleation.

## 6.2. Stresses in the Subducting Nazca Plate

The observed pattern of near-vertical P-axes within the near-vertical subducting slab (e.g., Portner et al., 2020; Rodríguez et al., 2020) indicates that the DFEs in the Peru-Brazil region are occurring predominantly under down-dip compression (DDC). This type of regime was already recognized for events with  $M_w > 5$  (see

Figure 3d), and our results now show that the same regime holds for a wider range of magnitudes ( $4.2 \leq M_w \leq 7.5$ ) (Figure 3e). Despite our solutions presenting more variability in B and T axes orientations, as discussed before, P-axes in general are near vertical, reflecting the predominance of normal faulting among our solutions and supporting a dominant DDC regime (Figure 3e). DDC is the dominant stress regime for subduction zones around the globe holding deep-focus seismicity ( $d > 400$  km) (Houston, 2015), and is mainly attributed to the lower mantle resisting penetration of the subducting plate under its own weight (Isacks & Molnar, 1971).

### 6.2.1. DDC and Flat-Slab Subduction

The Nazca plate (<50 Myr) is presently converging against the South American plate at a rate of  $\sim 7$  cm/yr (DeMets et al., 2010; Müller et al., 2008) (Figure 1a). Near the Peruvian coast, the Nazca plate initially sinks at an angle of nearly  $30^\circ$  until it reaches a depth of  $\sim 100$  km, after which it continues to subduct almost horizontally for nearly 700 km under northern Peru, and 500–600 km under central and southern Peru, to finally drop almost vertically ( $\sim 75^\circ$ ) down to MTZ depths. The locus of the DFEs is precisely at the bottom of this vertically subsiding segment of the slab (Gutscher et al., 2000; Kirby et al., 1995). Laterally, such geometry extends for  $\sim 1,500$  km in the NS direction, between  $2^\circ\text{S}$  and  $15^\circ\text{S}$ , and defines a flat slab segment within the Nazca plate (Bishop et al., 2017; Gutscher et al., 2000). The flat slab geometry seems to be directly linked to the subduction of overthickened oceanic crust, especially the Nazca Ridge to the south and, possibly, a postulated Inca Plateau to the north (Gutscher et al., 1999, 2000). The positive buoyancy of such anomalous features likely prevents the slab from sinking at an angle and keeps it moving horizontally until significant eclogitization occurs and becomes negatively buoyant (Antonijevic et al., 2015; Gutscher et al., 2000).

It's worth noting that the presence of an anomalously thick oceanic crust, although necessary, is not sufficient to explain flat subduction extending for more than 300 km from the trench. As demonstrated by previous modeling studies (e.g., Espurt et al., 2008; Manea et al., 2012), a combination of other effects such as trench retreat is required (Antonijevic et al., 2015). Seismic tomography studies also suggested that a marked slow velocity anomaly beneath the Peruvian flat slab, extending from 165 to 650 km depth and possibly reflecting hot and buoyant mantle material, might be supporting the observed flat geometry (e.g., Portner et al., 2017, 2020; Rodríguez et al., 2020; Scire et al., 2016). This support would explain why the Nazca slab remains flat far beyond the expected eclogitization limit ( $\sim 350$  km from the trench) (Bishop et al., 2017). Note that subduction velocity in the MTZ should be decreased due to flat slab subduction, effectively reducing slab penetration into the lower mantle, and possibly reducing the stresses associated with lower mantle resistance. If this were the case, we would expect relatively lower strain rates at MTZ depths, and buoyancy alone might not be strong enough to trigger DDC within the slab.

As demonstrated by independent numerical modeling studies, DDC is usually predicted at MTZ depths for a plate under both equilibrium and disequilibrium phase transformation conditions, the last one meaning the presence of metastable phase in the MTZ (e.g., Bina et al., 2001; Devaux et al., 2000; Guest et al., 2003). Under equilibrium conditions, DDC is expected to occur inside the subducting slab due to the buoyancy forces generated by the density contrasts at both top and bottom of the MTZ, which are caused by the elevation and depression of the main phase boundaries that define the MTZ. Under disequilibrium conditions, such a regime is also predicted by volumetric changes due to olivine phase transformations. Moreover, stresses from volumetric changes will dominate over buoyancy stresses (e.g., Devaux et al., 2000) becoming the most important source of stress behind DFEs. Because the slab should be considerably dehydrated after the anomalously long horizontal subduction—which goes far beyond the eclogitization limit—the persistence of a MOW could be making a significant contribution to the strain rates responsible for DFEs.

### 6.2.2. Viability of Transformational Faulting

Transformational faulting naturally requires the formation of new faults in the MOW, which would in turn be controlled by the slab stress field (Warren et al., 2007). According to Warren et al. (2007), conjugate ruptures in DDC regimes are expected to occur along planes oriented  $\pm\Phi$  from the slab dip (or from the P-axis),  $\Phi$  being the angle of internal friction (see their Figure 1). Their findings for the Tonga-Kermadec subduction zone suggest that  $\Phi$  is close to  $45^\circ$ , consistent with Anderson's prediction when no internal friction is acting on the fault plane and with other previous laboratory and seismological studies (Jiao et al., 2000; Kirby, 1987). To find the angle of internal friction, we first invert the principal stresses from the 39 GCMT solutions available in the Peru-Brazil

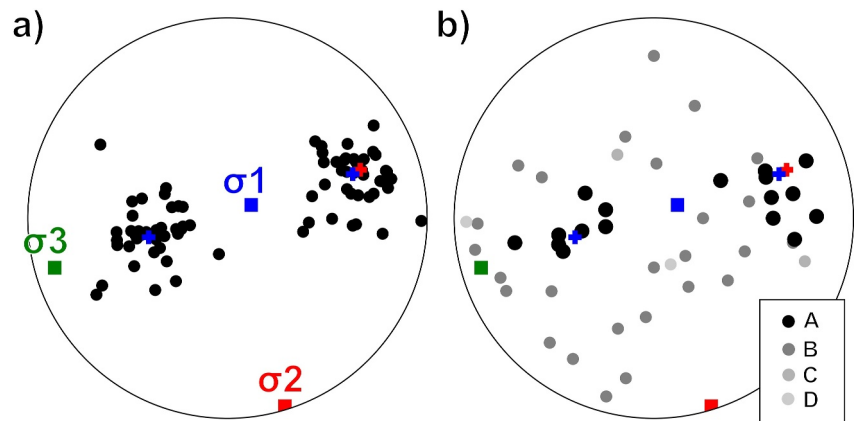


**Figure 6.** Nodal plane poles displayed on stereographic projection: (a) GCMT solutions (solid black circles) plotted with the inverted stresses (colored squares). The two fault planes poles predicted by the inverted stresses are plotted as blue crosses while the pole of the regional fault plane proposed by Zahradník et al. (2017) is plotted as a red cross; and (b) the same as in (a) but with solutions from this study colored according to quality.

segment, using the STRESSINVERSE package (Vavryčuk, 2014), which performs the inversion according to Michael's methodology (Michael, 1984, 1987). After that, we plot the conjugate plane poles predicted by these stresses. In Figure 6a the poles from GCMT solutions can be separated into two clusters, each of them centered around one of the two expected 45° planes, and the regional fault plane proposed by Zahradník et al. (2017) shows remarkable agreement with the relatively more vertical west-dipping plane. The histogram in Figure 7a shows that there is a marked concentration of GCMT nodal planes around 45° from the main compression axis. Thus, GCMT nodal planes are in reasonable agreement with fault planes expected from transformational faulting. Note, however, that this region lacks evidence of faulting along the east-dipping and more horizontal plane. In Figure 6b, A-quality solutions from this study are clearly clustering similar to those from the GCMT catalog, and there is also a clear concentration of nodal planes at ~45° (Figure 7b). B- to D-quality solutions show the previously explained variability, which can be due to uncertainties or to variations in the dominant stress field.

### 6.3. Thermal Structure and Deep-Focus Nucleation

For young and slow lithosphere deep seismicity is commonly restricted to less than 300 km depth (Myhill, 2013; Wortel, 1982). Assuming that DFEs are nucleated in a MOW within the subducting slab, the inability of such a hot lithosphere to preserve olivine at those depths would explain why deep-focus seismicity would be inhibited. As the Nazca plate is regarded as a warm endmember within the subduction zone spectrum (e.g., Frohlich, 2006; Wiens & Gilbert, 1996), deep-focus seismicity would not be expected. The thermal classification of the Nazca plate, however, is based on estimates of the thermal parameter, which characterizes the thermal structure of the whole plate based on its properties—subduction speed and age—at the trench (Frohlich, 2006) and does not characterize thermal structure in detail.

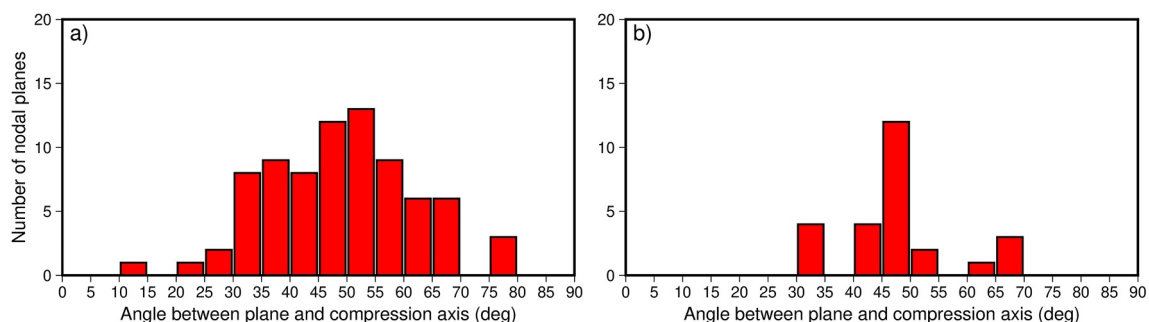


**Figure 7.** Histograms of the number of nodal planes as a function of the angle between these planes and the main compression axis. (a) Histogram considering only GCMT solutions for the study region and (b) considering only A-quality solutions obtained in this study.

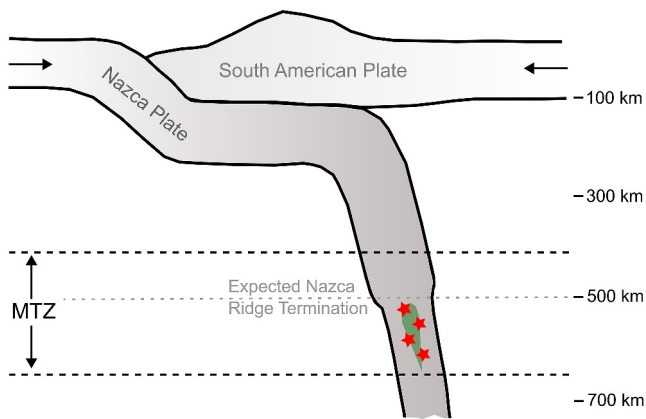


**Figure 8.** Schematic model proposed to explain deep-focus seismicity in the Peru-Brazil region. The model illustrates the South American subduction zone and the main features observed in the study region, the Peruvian flat slab, and the concentration of DFEs in a narrow fault zone. The Nazca ridge termination, as suggested by Bishop et al. (2017), is indicated by the red dashed line at ~500 km depth. The ridge termination marks the transition from a warmer to a colder Nazca slab segment. In the colder segment, we propose that a MOW could be preserved and thus allowing for earthquake nucleation (red stars) in the MTZ.

### 6.3.1. Composite Thermal Structure at the Peru-Brazil Border

Kirby et al. (1995), in their study of the great 1994 Bolivian earthquake, noted that the Nazca plate might have an anomalous thermal structure, consisting of a hot upper portion and a cold lower portion. Such composite structure would have resulted from the juxtaposition of younger, Tertiary-age lithosphere currently entering the trench and older, Mesozoic-age lithosphere in the deeper portions of the slab. According to Okal and Bina (1994) the older portion would have originated at the Pacific-Farallon spreading center at ~50–65 Ma and would be presently sitting at 500–700 km depth. The idea, first suggested by Engebretson and Kirby (1992), would thus explain the composite thermal structure through abrupt variation in slab age.

Alternatively, the composite thermal structure could be the result of a reduction in subduction velocity due to subduction of the Nazca ridge. Aseismic ridges, which are characterized by anomalously thick oceanic crust, have been invoked to explain segmentation by flat-slab subduction along the South American Pacific border (Espurt et al., 2008; Gutscher et al., 2000; Hu et al., 2016; McGeary et al., 1985), and might in turn have been responsible for slowing subduction along those segments due to their enhanced buoyancy (Espurt et al., 2008). In the Peru-Brazil region, it has been estimated that the tip of the aseismic Nazca Ridge would currently be at ~500 km depth (Bishop et al., 2017). In this alternative scenario, the composite thermal structure would be the result of a warm upper portion from slow, flat-style subduction

juxtaposed to a cold lower portion from faster (and older), normal-style subduction (Collier & Helffrich, 2001; Engebretson & Kirby, 1992; Kirby et al., 1995; Okal & Bina, 1994).

Regardless of the nature of the postulated composite thermal structure, an abrupt transition from warm to cold is thus to be expected at around 500 km depth. Interestingly, one of the main findings of this study is that deep-focus seismicity along the Peru-Brazil border is confined between 557 and 659 km depth (557 and 642 if only A-quality solutions are considered) within the Nazca slab, well beyond the depth at which the abrupt thermal transition is postulated (Table 2). The concentration of deep-focus seismicity below 500 km depth, and the corresponding paucity above that depth, is consistent with the composite thermal structure mentioned above (Engebretson & Kirby, 1992; Kirby et al., 1995). The deeper and colder portion of the slab may have remained sufficiently cold during subduction to preserve olivine metastably down to MTZ depths, while the shallower and warmer portion may have inhibited metastability and completely transformed olivine aseismically near the nominal equilibrium depth. The preservation of a MOW in the deeper portion would have permitted the nucleation of DFEs through transformational faulting while the lack of a MOW in the shallower portion would have prevented their nucleation (Figure 8).

Moreover, if the composite thermal structure were correct, mechanisms commonly proposed for colder slabs (i.e., transformational faulting) would also become viable for the nominally warmer Nazca slab. Realize that even a thin MOW would be sufficient to nucleate deep-focus ruptures, as they could propagate beyond the MOW through some complementary mechanism such as thermal runaway (Zhan, 2017). A recent experiment has demonstrated that after a rupture is initiated by transformational faulting, it can propagate outside from the metastable nucleus when accompanied by melting (Gasc et al., 2022). Indeed, the largest deep-focus ruptures in South America have been explained through this dual-mechanism. For the Bolivia earthquake of 1994 (Mw 8.2 and 637 km), for example, the extremely low seismic efficiency determined by Kanamori et al. (1998) clearly attests to a very dissipative process during its rupture, possibly involving melting.

Alternatively, Billen (2020) suggested that the large gaps in deep-focus seismicity observed in South America and Java-Sumatra could be explained through a combination of regions of high strain rates and cold temperatures within the slab. The seismic gaps observed in many subduction zones would thus be the result of sluggish deformation rather than high temperature alone. Similarly, the abrupt paucity in seismicity around the top of the more viscous lower mantle could be due to minimum strain rates predicted at such depths. For the Peruvian and Chilean segments, for example, high strain rates could explain the concentration of events at around 600 km,

probably due to phase transformations around those depths. Slab temperature, nonetheless, would still be a major factor influencing slab rheology, as warmer slabs would be expected to deform more plastically (Billen, 2020).

### 6.3.2. A Generalized, Composite Thermal Structure for South America?

Along the whole of the South America subduction front, deep-focus seismicity is clearly limited to regions where the subducting Nazca plate is imaged at depth. Some tomography models show that the Nazca plate is continuous from the north of Peru down to central Argentina, comprising the observed deep-focus segments (see models SAM5\_P\_2019, UU\_P07, MITP08, and DETOX-P1 in Figure 9 from Mohammadzahari et al. (2021)) (Amaru, 2007; C. Li et al., 2008; Mohammadzahari et al., 2021; Portner et al., 2020). The apparent absence of this oceanic lithosphere further north and south could explain the absence of deep-focus seismicity in these regions. Additionally, it has been demonstrated that the Nazca plate does penetrate the lower mantle all along its strike, which would in turn explain the predominant DDC regime for these kind of earthquakes in South America (Portner et al., 2020).

As with the Peru-Brazil segment, it is possible that a thermally composite Nazca plate may be responsible for allowing DFEs in other segments as well. In Figure 1a, it is notable that the subduction of three aseismic ridges (Nazca, Iquique, and Juan Fernandez) seems to be related to the distribution of deep earthquakes with depth. Note that regions characterized by the subduction of these anomalously thick oceanic crusts are displaying marked gaps in deep seismicity, from nearly 200 to ~500/600 km: In Peru, related to the Nazca Ridge; in central Bolivia, related to the Iquique Ridge; and in central Chile, related to the Juan Fernandez Ridge. Another marked gap is also observed further north of the Chilean-Pampean flat-slab, which could be associated with the subduction of the Copiapó Ridge. Although the Chilean-Pampean flat slab is often attributed to the subduction of the Juan Fernandez Ridge alone, it is possible that the Copiapó Ridge also contributed to the formation of this feature at its northern limit (Álvarez et al., 2015; Gimenez et al., 2019). Other regions, on the other hand, show almost continuous distributions of events with depth (see, for instance, northern Chile and southern Bolivia).

Note, however, that flat subduction is only observed in Peru and central Chile, linked to the subduction of the Nazca Ridge and Juan Fernandez Ridge. The subduction of the Carnegie and Iquique Ridges, on the other hand, is not associated to flat subduction, probably because the subduction of such features began too recently (1–2 Ma ago) (Espurt et al., 2008). In Central Bolivia, where the Iquique Ridge is subducting, a marked gap in deep seismicity is observed, flanked by two regions with continuous distribution of earthquakes (Figure 1a). In this case, it is possible that the plate is currently under a slab flattening process (Espurt et al., 2008). This process could be now reducing subduction velocity and consequently increasing temperatures in the oceanic plate but, as slab flattening is not complete, it is not clear if our model could explain seismicity in this region. It is notable that this region is marked by very few available mechanisms (Figure 1a). In fact, regions marked by flat subduction are presenting higher seismic activity in the MTZ compared to this Northern Bolivia-Peru segment (see the Peru-Brazil and Northern Argentina-Bolivia segments of deep-focus seismicity in Figure 1).

## 7. Conclusions

In this work we determined focal mechanisms and centroid depths for a total of 28 DFEs that occurred in the Peru-Brazil region from 2014 to 2022. This sequence included the great 2015 Mw 7.5 doublet and its aftershocks. We observed a predominant pattern of normal faults in our solutions, describing a pattern of near-vertical P-axis, strike-parallel B-axis, and slab-normal T axis consistent with DDC within the Nazca slab. We also observed some normal solutions deviating from this general pattern, probably resulting from local stress changes brought by larger events, as well as more severe variations in faulting style that include oblique strike-slip and an oblique reverse mechanisms. The DDC regime is consistent with other regions in the world hosting deep-focus seismicity and we observed that this regime holds for a wider range of magnitudes ( $4.2 \leq M_w \leq 7.5$ ) than previously observed ( $M_w > 5$ ).

The observed stress regime is consistent with both equilibrium and disequilibrium conditions within the subducting slab, and thus does not necessarily imply the existence of a MOW. Nevertheless, the expected influence of the flat-slab subduction in the stress regime and the observation of fault-plane orientations at  $\sim 45^\circ$  from the main axis of compression—suggesting they are consistent with newly formed faults—is found consistent with transformational faulting on a MOW. The viability of transformational faulting in a MOW is discussed in the light of a thermally composite Nazca slab. In this hypothesis, the young and warmer Nazca plate that is being subducted is

attached at ~500 km to an older and colder lithosphere segment in the MTZ. This thermal anomaly would be responsible for allowing metastable material to penetrate deep into the MTZ, and consequently allowing for transformational faulting to occur. This would explain the observed narrow band of deep-focus seismicity and could also explain both the pronounced seismic gap at ~300–500 km, where the warmer slab is subducting, and the lack of seismicity at the top of the lower mantle.

## Data Availability Statement

All seismograms used in this work were collected from a variety of sources and are made available at a Zenodo repository (<https://doi.org/10.5281/ZENODO.10685297>) (Leite Neto et al., 2024). Data from the permanent Brazilian Seismographic Network (RSBR, comprising network codes BL, BR, NB, and ON) are distributed at <http://rsbr.on.br> (Observatório Nacional, Rio de Janeiro, RJ, 2011), while data from the temporary 3-basins Project (network code XC) can be obtained through the USP Seismological Center (USPSC) FDSNWS server (<http://seisrequest.iag.usp.br/fdsnws/dataselect/1/>) (Assumpção & Bianchi, 2016). Seismic data from the other networks were all acquired through the EarthScope Consortium Wilber 3 system (<https://ds.iris.edu/wilber3/>), including networks: IU (Albuquerque Seismological Laboratory/USGS, 2014), II (Scripps Institution of Oceanography, 1986), G (Institut de Physique du Globe de Paris (IPGP) and École et Observatoire des Sciences de la Terre de Strasbourg (EOST), 1982), GE (GEOFON Data Centre, 1993), C (Chilean National Seismic Network), C1 (Universidad de Chile, 2012), CX (GFZ German Research Centre for Geosciences; Institut des Sciences De l'Univers-Centre National de la Recherche CNRS-INSU, 2006), CM (Servicio Geológico Colombiano, 1993) and EC (Ecuador Seismic Network). Several figures in this manuscript were generated using PyGMT (Uieda et al., 2022; Wessel et al., 2019).

## Acknowledgments

We express our gratitude to J. Zahradník and an anonymous reviewer for providing valuable comments and suggestions that improved the clarity of this manuscript. We thank M. Assumpção, M. Bianchi, and B. Collaço for facilitating access to data from the temporary XC network. We also thank C.J. Ammon for making his inversion codes available. GSLN was supported by the Coordenação de Aperfeiçoamento de Pessoal de Nível Superior—Brasil (CAPES)—Finance Code 001, through a PhD scholarship at the Universidade Federal do Rio Grande do Norte (UFRN) and a exchange scholarship (Programa de Doutorado Sanduíche no Exterior—PDSE/CAPES) to study at Universidad Nacional de Colombia (UNAL). JJ also thanks the Conselho Nacional de Desenvolvimento Científico e Tecnológico (CNPq) for support through a research Grant (award no. 434807/2018-4) and a continued research fellowship (award no. 310261/2023-6).

## References

- Albuquerque Seismological Laboratory/USGS. (2014). Global Seismograph Network (GSN—IRIS/USGS) [Dataset]. *International Federation of Digital Seismograph Networks*. <https://doi.org/10.7914/SN/IU>
- Allmendinger, R. W., Cardozo, N., & Fisher, D. M. (2012). *Structural geology algorithms: Vectors and tensors*. Cambridge University Press.
- Álvarez, O., Gimenez, M., Folguera, A., Spagnotto, S., Bustos, E., Baez, W., & Braitenberg, C. (2015). New evidence about the subduction of the Copiapó ridge beneath South America, and its connection with the Chilean-Pampean flat slab, tracked by satellite GOCE and EGM2008 models. *Journal of Geodynamics*, 91, 65–88. <https://doi.org/10.1016/j.jog.2015.08.002>
- Álvarez-Gómez, J. A. (2019). FMC—Earthquake focal mechanisms data management, cluster and classification. *SoftwareX*, 9, 299–307. <https://doi.org/10.1016/j.softx.2019.03.008>
- Amaru, M. L. (2007). *Global travel time tomography with 3-D reference models*. Utrecht University.
- Antonijevec, S. K., Wagner, L. S., Kumar, A., Beck, S. L., Long, M. D., Zandt, G., et al. (2015). The role of ridges in the formation and longevity of flat slabs. *Nature*, 524(7564), 212–215. <https://doi.org/10.1038/nature14648>
- Assumpção, M., Bianchi, M., Rocha, M., & Azevedo, P. A. D. (2016). The “3-basins” project in mid South America and the geometry of the deep Nazca subducted slab. In *American geophysical union, fall meeting 2016*.
- Assumpção, M. S., & Bianchi, M. B. (2016). Pantanal, Chaco and Paraná (PCPB) structural studies network [Dataset]. *USP Seismological Center (USPSC)*. <https://doi.org/10.7914/8scf-yd39>
- Bianchi, M. B., Assumpção, M., Rocha, M. P., Carvalho, J. M., Azevedo, P. A., Fontes, S. L., et al. (2018). The Brazilian seismographic network (RSBR): Improving seismic monitoring in Brazil. *Seismological Research Letters*, 89(2A), 452–457. <https://doi.org/10.1785/0220170227>
- Billen, M. I. (2020). Deep slab seismicity limited by rate of deformation in the transition zone. *Science Advances*, 6(22). <https://doi.org/10.1126/sciadv.aaz7692>
- Bina, C. R., Stein, S., Marton, F. C., & Van Ark, E. M. (2001). Implications of slab mineralogy for subduction dynamics. *Physics of the Earth and Planetary Interiors*, 127(1–4), 51–66. [https://doi.org/10.1016/S0031-9201\(01\)00221-7](https://doi.org/10.1016/S0031-9201(01)00221-7)
- Bird, P. (2003). An updated digital model of plate boundaries. *Geochemistry, Geophysics, Geosystems*, 4(3), 1027. <https://doi.org/10.1029/2001GC000252>
- Bishop, B. T., Beck, S. L., Zandt, G., Wagner, L., Long, M., Antonijevec, S. K., et al. (2017). Causes and consequences of flat-slab subduction in southern Peru. *Geosphere*, 13(5), 1392–1407. <https://doi.org/10.1130/GES01440.1>
- Bouchon, M. (1981). A simple method to calculate Green's functions for elastic layered media. *Bulletin of the Seismological Society of America*, 71(4), 959–971. <https://doi.org/10.1785/BSSA0710040959>
- Čejka, F., Zahradník, J., Turhan, F., Sokos, E., & Gallovič, F. (2023). Long-period directivity pulses of strong ground motion during the 2023 Mw7.8 Kahramanmaraş earthquake. *Communications Earth & Environment*, 4(1), 413. <https://doi.org/10.1038/s43247-023-01076-x>
- Chagas de Melo, B., & Assumpção, M., & “3-Basins” Project Team. (2018). Mantle anisotropy and asthenospheric flow around cratons in southeastern South America. *Geophysical Journal International*, 215(1), 494–506. <https://doi.org/10.1093/gji/ggy288>
- Chang, Y., Warren, L. M., Zhu, L., & Prieto, G. A. (2019). Earthquake focal mechanisms and stress field for the intermediate-depth Cauca cluster, Colombia. *Journal of Geophysical Research: Solid Earth*, 124(1), 822–836. <https://doi.org/10.1029/2018JB016804>
- Chu, R., Zhu, L., & HelMBERGER, D. V. (2009). Determination of earthquake focal depths and source time functions in central Asia using teleseismic P waveforms. *Geophysical Research Letters*, 36(L17317), 1–4. <https://doi.org/10.1029/2009GL039494>
- Collier, J. D., & Helffrich, G. R. (2001). The thermal influence of the subducting slab beneath South America from 410 and 660 km discontinuity observations. *Geophysical Journal International*, 147(2), 319–329. <https://doi.org/10.1046/j.1365-246X.2001.00532.x>
- Crotwell, H. P., Owens, T. J., & Ritsema, G. (1999). The TauP toolkit: Flexible seismic travel-time and ray-path utilities. *Seismological Research Letters*, 70(2), 154–160. <https://doi.org/10.1785/gssrl.70.2.154>

- DeMets, C., Gordon, R. G., & Argus, D. F. (2010). Geologically current plate motions. *Geophysical Journal International*, *181*(1), 1–80. <https://doi.org/10.1111/j.1365-246X.2009.04491.x>
- Devaux, J. P., Fleitout, L., Schubert, G., & Anderson, C. (2000). Stresses in a subducting slab in the presence of a metastable olivine wedge. *Journal of Geophysical Research*, *105*(B6), 13365–13373. <https://doi.org/10.1029/1999JB900274>
- Devaux, J. P., Schubert, G., & Anderson, C. (1997). Formation of a metastable olivine wedge in a descending slab. *Journal of Geophysical Research*, *102*(B11), 24627–24637. <https://doi.org/10.1029/97JB02334>
- Du Frane, W. L., Sharp, T. G., Mosenfelder, J. L., & Leinenweber, K. (2013). Ringwoodite growth rates from olivine with ~75ppmw H<sub>2</sub>O: Metastable olivine must be nearly anhydrous to exist in the mantle transition zone. *Physics of the Earth and Planetary Interiors*, *219*, 1–10. <https://doi.org/10.1016/j.pepi.2013.04.001>
- Dziewonski, A. M., Chou, T.-A., & Woodhouse, J. H. (1981). Determination of earthquake source parameters from waveform data for studies of global and regional seismicity. *Journal of Geophysical Research*, *86*(B4), 2825–2852. <https://doi.org/10.1029/JB086iB04p02825>
- Ekström, G., Nettles, M., & Dziewoński, A. M. (2012). The global CMT project 2004–2010: Centroid-moment tensors for 13,017 earthquakes. *Physics of the Earth and Planetary Interiors*, *200–201*, 1–9. <https://doi.org/10.1016/j.pepi.2012.04.002>
- Engelbreton, D. C., & Kirby, S. H. (1992). Deep Nazca slab seismicity: Why is it so anomalous? *Eos, Transactions, American Geophysical Union*, *73*(43), 379. [abstract].
- Espurt, N., Funicicello, F., Martinod, J., Guillaume, B., Regard, V., Faccenna, C., & Brusset, S. (2008). Flat subduction dynamics and deformation of the South American plate: Insights from analog modeling. *Tectonics*, *27*(TC3011). <https://doi.org/10.1029/2007TC002175>
- Frohlich, C. (1989). The nature of deep-focus earthquakes. *Annual Review of Earth and Planetary Sciences*, *17*(1), 227–254. <https://doi.org/10.1146/annurev.earth.17.1.227>
- Frohlich, C. (1994). Earthquakes with non-double-couple mechanisms. *Science*, *264*(5160), 804–809. <https://doi.org/10.1126/science.264.5160.804>
- Frohlich, C. (2006). *Deep earthquakes*. Cambridge University Press. <https://doi.org/10.1017/CBO9781107297562>
- Gasc, J., Daigne, C., Moarefvand, A., Deldicque, D., Fauconnier, J., Gardonio, B., et al. (2022). Deep-focus earthquakes: From high-temperature experiments to cold slabs. *Geology*, *50*(9), 1018–1022. <https://doi.org/10.1130/G50084.1>
- GEOFON Data Centre. (1993). GEOFON seismic network [Dataset]. *Deutsches GeoForschungszentrum GFZ*. <https://doi.org/10.14470/TR560404>
- GFZ German Research Centre for Geosciences; Institut des Sciences De l'Univers-Centre National de la Recherche CNRS-INSU. (2006). IPOC seismic network [Dataset]. *Integrated Plate boundary Observatory Chile—IPOC*. <https://doi.org/10.14470/PK615318>
- Gimenez, M., Acosta, G., Alvarez, O., Pesce, A., Lince Kingler, F., & Folguera, A. (2019). The subduction of the Copiapó aseismic ridge, is the causing of the formation of metallic minerals deposits in north of Chile and Argentina? *Geodesy and Geodynamics*, *10*(6), 471–476. <https://doi.org/10.1016/j.geog.2019.04.007>
- Green, H. W., & Burnley, P. C. (1989). A new self-organizing mechanism for deep-focus earthquakes. *Nature*, *341*(6244), 733–737. <https://doi.org/10.1038/341733a0>
- Green, H. W., & Marone, C. (2002). Instability of deformation. *Reviews in Mineralogy and Geochemistry*, *51*(1), 181–199. <https://doi.org/10.2138/gsrmg.51.1.181>
- Green, H. W., & Zhou, Y. (1996). Transformation-induced faulting requires an exothermic reaction and explains the cessation of earthquakes at the base of the mantle transition zone. *Tectonophysics*, *256*(1–4), 39–56. [https://doi.org/10.1016/0040-1951\(95\)00164-6](https://doi.org/10.1016/0040-1951(95)00164-6)
- Guest, A., Schubert, G., & Gable, C. W. (2003). Stress field in the subducting lithosphere and comparison with deep earthquakes in Tonga. *Journal of Geophysical Research*, *108*(B6), 2288. <https://doi.org/10.1029/2002JB002161>
- Gutscher, M.-A., Olivet, J.-L., Aslanian, D., Eissen, J.-P., & Maury, R. (1999). The “lost Inca Plateau”: Cause of flat subduction beneath Peru? *Earth and Planetary Science Letters*, *171*(3), 335–341. [https://doi.org/10.1016/S0012-821X\(99\)00153-3](https://doi.org/10.1016/S0012-821X(99)00153-3)
- Gutscher, M.-A., Spakman, W., Bijwaard, H., & Engdahl, E. R. (2000). Geodynamics of flat subduction: Seismicity and tomographic constraints from the Andean margin. *Tectonics*, *19*(5), 814–833. <https://doi.org/10.1029/1999TC001152>
- Hanks, T. C., & Kanamori, H. (1979). A moment magnitude scale. *Journal of Geophysical Research*, *84*(B5), 2348–2350. <https://doi.org/10.1029/JB084iB05p02348>
- Hayes, G. P., Moore, G. L., Portner, D. E., Hearne, M., Flamme, H., Furtney, M., & Smoczyk, G. M. (2018). Slab2, a comprehensive subduction zone geometry model. *Science*, *362*(6410), 58–61. <https://doi.org/10.1126/science.aat4723>
- Herrmann, R. B. (2013). Computer programs in seismology: An evolving tool for instruction and research. *Seismological Research Letters*, *84*(6), 1081–1088. <https://doi.org/10.1785/0220110096>
- Heyburn, R., Selby, N. D., & Fox, B. (2013). Estimating earthquake source depths by combining surface wave amplitude spectra and teleseismic depth phase observations. *Geophysical Journal International*, *194*(2), 1000–1010. <https://doi.org/10.1093/gji/ggt140>
- Hogrefe, A., Rubie, D. C., Sharp, T. G., & Seifert, F. (1994). Metastability of enstatite in deep subducting lithosphere. *Nature*, *372*(6504), 351–353. <https://doi.org/10.1038/372351a0>
- Hosoya, T., Kubo, T., Ohtani, E., Sano, A., & Funakoshi, K. (2005). Water controls the fields of metastable olivine in cold subducting slabs. *Geophysical Research Letters*, *32*(L17305), L17305. <https://doi.org/10.1029/2005GL023398>
- Houston, H. (2015). Deep earthquakes. In *Treatise on geophysics* (pp. 329–354). Elsevier. <https://doi.org/10.1016/B978-0-444-53802-4.00079-8>
- Hu, J., Liu, L., Hermosillo, A., & Zhou, Q. (2016). Simulation of late Cenozoic South American flat-slab subduction using geodynamic models with data assimilation. *Earth and Planetary Science Letters*, *438*, 1–13. <https://doi.org/10.1016/j.epsl.2016.01.011>
- Institut de Physique du Globe de Paris (IPGP) and École et Observatoire des Sciences de la Terre de Strasbourg (EOST). (1982). GEOSCOPE, French global network of broad band seismic stations [Dataset]. *Institut de Physique du Globe de Paris (IPGP), Université de Paris*. <https://doi.org/10.18715/GEOSCOPE.G>
- Isacks, B., & Molnar, P. (1971). Distribution of stresses in the descending lithosphere from a global survey of focal-mechanism solutions of mantle earthquakes. *Reviews of Geophysics*, *9*(1), 103–174. <https://doi.org/10.1029/RG009i001p0103>
- Ishii, T., & Ohtani, E. (2021). Dry metastable olivine and slab deformation in a wet subducting slab. *Nature Geoscience*, *14*(7), 526–530. <https://doi.org/10.1038/s41561-021-00756-7>
- Jiao, W., Silver, P. G., Fei, Y., & Prewitt, C. T. (2000). Do intermediate- and deep-focus earthquakes occur on preexisting weak zones? An examination of the Tonga subduction zone. *Journal of Geophysical Research*, *105*(B12), 28125–28138. <https://doi.org/10.1029/2000JB900314>
- Jiménez, C., Calvo, C., Saavedra, M., Moggiano, N., & Molina, W. (2021). Source characteristics of Peruvian deep focus seismic doublet of November 24, 2015. *Journal of South American Earth Sciences*, *105*, 102919. <https://doi.org/10.1016/j.jsames.2020.102919>
- Kanamori, H., Anderson, D. L., & Heaton, T. H. (1998). Frictional melting during the rupture of the 1994 Bolivian earthquake. *Science*, *279*(5352), 839–842. <https://doi.org/10.1126/science.279.5352.839>

- Kaverina, A. N., Lander, A. V., & Prozorov, A. G. (1996). Global creep distribution and its relation to earthquake-source geometry and tectonic origin. *Geophysical Journal International*, 125(1), 249–265. <https://doi.org/10.1111/j.1365-246X.1996.tb06549.x>
- Kawakatsu, H. (1991). Insignificant isotropic component in the moment tensor of deep earthquakes. *Nature*, 351(6321), 50–53. <https://doi.org/10.1038/351050a0>
- Kelemen, P. B., & Hirth, G. (2007). A periodic shear-heating mechanism for intermediate-depth earthquakes in the mantle. *Nature*, 446(7137), 787–790. <https://doi.org/10.1038/nature05717>
- Kennett, B. L. N., Engdahl, E. R., & Buland, R. (1995). Constraints on seismic velocities in the Earth from traveltimes. *Geophysical Journal International*, 122(1), 108–124. <https://doi.org/10.1111/j.1365-246X.1995.tb03540.x>
- Kirby, S. H. (1987). Localized polymorphic phase transformations in high-pressure faults and applications to the physical mechanism of deep earthquakes. *Journal of Geophysical Research*, 92(B13), 13789–13800. <https://doi.org/10.1029/JB092iB13p13789>
- Kirby, S. H., Durham, W. B., & Stern, L. A. (1991). Mantle phase changes and deep-earthquake faulting in subducting lithosphere. *Science*, 252(5003), 216–225. <https://doi.org/10.1126/science.252.5003.216>
- Kirby, S. H., Okal, E. A., & Engdahl, E. R. (1995). The 9 June 94 Bolivian deep earthquake: An exceptional event in an extraordinary subduction zone. *Geophysical Research Letters*, 22(16), 2233–2236. <https://doi.org/10.1029/95GL01802>
- Kubo, T., Ohtani, E., Kato, T., Shinmei, T., & Fujino, K. (1998). Effects of water on the  $\alpha$ - $\beta$  transformation kinetics in San Carlos olivine. *Science*, 281(5373), 85–87. <https://doi.org/10.1126/science.281.5373.85>
- Leite Neto, G., Julià, J., & Prieto, G. (2024). Seismograms for deep-focus earthquakes in the Peru-Brazil region [Dataset]. *Zenodo*. <https://doi.org/10.5281/ZENODO.10685297>
- Leite Neto, G. S., & Julià, J. (2023). Determination of intraplate focal mechanisms with the Brazilian Seismic Network: A simplified Cut-and-Paste approach. *Journal of South American Earth Sciences*, 121, 104149. <https://doi.org/10.1016/j.jsames.2022.104149>
- Li, C., Van der Hilst, R. D., Engdahl, E. R., & Burdick, S. (2008). A new global model for P wave speed variations in Earth's mantle. *Geochemistry, Geophysics, Geosystems*, 9(5), Q05018. <https://doi.org/10.1029/2007GC001806>
- Li, J., Zheng, Y., Thomsen, L., Lapen, T. J., & Fang, X. (2018). Deep earthquakes in subducting slabs hosted in highly anisotropic rock fabric. *Nature Geoscience*, 11(9), 696–700. <https://doi.org/10.1038/s41561-018-0188-3>
- Manea, V. C., Pérez-Gussinyé, M., & Manea, M. (2012). Chilean flat slab subduction controlled by overriding plate thickness and trench rollback. *Geology*, 40(1), 35–38. <https://doi.org/10.1130/G32543.1>
- Mao, G. L., Ferrand, T. P., Li, J., Zhu, B., Xi, Z., & Chen, M. (2022). Unsupervised machine learning reveals slab hydration variations from deep earthquake distributions beneath the northwest Pacific. *Communications Earth & Environment*, 3(56), 1–9. <https://doi.org/10.1038/s43247-022-00377-x>
- Marrett, R., & Allmendinger, R. W. (1990). Kinematic analysis of fault-slip data. *Journal of Structural Geology*, 12(8), 973–986. [https://doi.org/10.1016/0191-8141\(90\)90093-E](https://doi.org/10.1016/0191-8141(90)90093-E)
- McGeary, S., Nur, A., & Ben-Avraham, Z. (1985). Spatial gaps in arc volcanism: The effect of collision or subduction of oceanic plateaus. *Tectonophysics*, 119(1–4), 195–221. [https://doi.org/10.1016/0040-1951\(85\)90039-3](https://doi.org/10.1016/0040-1951(85)90039-3)
- Michael, A. J. (1984). Determination of stress from slip data: Faults and folds. *Journal of Geophysical Research*, 89(B13), 11517–11526. <https://doi.org/10.1029/JB089iB13p11517>
- Michael, A. J. (1987). Use of focal mechanisms to determine stress: A control study. *Journal of Geophysical Research*, 92(B1), 357–368. <https://doi.org/10.1029/JB092iB01p00357>
- Miller, R. G. (1974). The jackknife—A review. *Biometrika*, 61(1), 1–15. <https://doi.org/10.2307/2334280>
- Mohammadzahari, A., Sigloch, K., Hosseini, K., & Mihalynuk, M. G. (2021). Subducted lithosphere under South America from multifrequency P wave tomography. *Journal of Geophysical Research: Solid Earth*, 126(6), e2020JB020704. <https://doi.org/10.1029/2020JB020704>
- Montagner, J.-P., & Kennett, B. L. N. (1996). How to reconcile body-wave and normal-mode reference Earth models. *Geophysical Journal International*, 125(1), 229–248. <https://doi.org/10.1111/j.1365-246X.1996.tb06548.x>
- Mosenfelder, J. L., Marton, F. C., Ross, C. R., Kerschhofer, L., & Rubie, D. C. (2001). Experimental constraints on the depth of olivine metastability in subducting lithosphere. *Physics of the Earth and Planetary Interiors*, 127(1–4), 165–180. [https://doi.org/10.1016/S0031-9201\(01\)00226-6](https://doi.org/10.1016/S0031-9201(01)00226-6)
- Müller, R. D., Sdrolias, M., Gaina, C., & Roest, W. R. (2008). Age, spreading rates, and spreading asymmetry of the world's ocean crust. *Geochemistry, Geophysics, Geosystems*, 9(4), Q04006. <https://doi.org/10.1029/2007GC001743>
- Myhill, R. (2013). Slab buckling and its effect on the distributions and focal mechanisms of deep-focus earthquakes. *Geophysical Journal International*, 192(2), 837–853. <https://doi.org/10.1093/gji/ggs054>
- Observatório Nacional, Rio de Janeiro, RJ. (2011). Rede Sismográfica do Sul e do Sudeste [Dataset]. *International Federation of Digital Seismograph Networks*. <https://doi.org/10.7914/SN/ON>
- Ogawa, M. (1987). Shear instability in a viscoelastic material as the cause of deep focus earthquakes. *Journal of Geophysical Research*, 92(B13), 13801–13810. <https://doi.org/10.1029/JB092iB13p13801>
- Okal, E. A., & Bina, C. R. (1994). The deep earthquakes of 1921–1922 in Northern Peru. *Physics of the Earth and Planetary Interiors*, 87(1–2), 33–54. [https://doi.org/10.1016/0031-9201\(94\)90020-5](https://doi.org/10.1016/0031-9201(94)90020-5)
- Portner, D. E., Beck, S., Zandt, G., & Scire, A. (2017). The nature of subslab slow velocity anomalies beneath South America. *Geophysical Research Letters*, 44(10), 4747–4755. <https://doi.org/10.1002/2017GL073106>
- Portner, D. E., Rodríguez, E. E., Beck, S., Zandt, G., Scire, A., Rocha, M. P., et al. (2020). Detailed structure of the subducted Nazca slab into the lower mantle derived from continent-scale teleseismic P wave tomography. *Journal of Geophysical Research: Solid Earth*, 125(5), e2019JB017884. <https://doi.org/10.1029/2019JB017884>
- Quenouille, M. H. (1949). Approximate tests of correlation in time-series 3. *Mathematical Proceedings of the Cambridge Philosophical Society*, 45(3), 483–484. <https://doi.org/10.1017/S0305004100025123>
- Quenouille, M. H. (1956). Notes on bias in estimation. *Biometrika*, 43(3/4), 353–360. <https://doi.org/10.2307/2332914>
- Rodríguez, E. E., Portner, D. E., Beck, S. L., Rocha, M. P., Bianchi, M. B., Assumpção, M., et al. (2020). Mantle dynamics of the Andean Subduction Zone from continent-scale teleseismic S-wave tomography. *Geophysical Journal International*, 224(3), 1553–1571. <https://doi.org/10.1093/gji/ggaa536>
- Rosenbaum, G., Giles, D., Saxon, M., Betts, P. G., Weinberg, R. F., & Duboz, C. (2005). Subduction of the Nazca Ridge and the Inca Plateau: Insights into the formation of ore deposits in Peru. *Earth and Planetary Science Letters*, 239(1–2), 18–32. <https://doi.org/10.1016/j.epsl.2005.08.003>
- Ruiz, S., Tavera, H., Poli, P., Herrera, C., Flores, C., Rivera, E., & Madariaga, R. (2017). The deep Peru 2015 doublet earthquakes. *Earth and Planetary Science Letters*, 478, 102–109. <https://doi.org/10.1016/j.epsl.2017.08.036>

- Scire, A., Zandt, G., Beck, S., Long, M., Wagner, L., Minaya, E., & Tavera, H. (2016). Imaging the transition from flat to normal subduction: Variations in the structure of the Nazca slab and upper mantle under southern Peru and northwestern Bolivia. *Geophysical Journal International*, 204(1), 457–479. <https://doi.org/10.1093/gji/ggv452>
- Scripps Institution of Oceanography. (1986). Global Seismographic Network—IRIS/IDA [Dataset]. *International Federation of Digital Seismograph Networks*. <https://doi.org/10.7914/SN/II>
- Servicio Geológico Colombiano. (1993). Red Sismologica Nacional de Colombia [Dataset]. *International Federation of Digital Seismograph Networks*. <https://doi.org/10.7914/SN/CM>
- Tibi, R., Bock, G., & Wiens, D. A. (2003). Source characteristics of large deep earthquakes: Constraint on the faulting mechanism at great depths. *Journal of Geophysical Research*, 108(B2), 2091. <https://doi.org/10.1029/2002JB001948>
- Uieda, L., Tian, D., Leong, W. J., Jones, M., Schlitzer, W., Grund, M., et al. (2022). PyGMT: A Python interface for the generic mapping tools [Software]. *Zenodo*. <https://doi.org/10.5281/zenodo.7481934>
- Universidad de Chile. (2012). Red Sismologica Nacional [Dataset]. *International Federation of Digital Seismograph Networks*. <https://doi.org/10.7914/SN/C1>
- Vavryčuk, V. (2014). Iterative joint inversion for stress and fault orientations from focal mechanisms. *Geophysical Journal International*, 199(1), 69–77. <https://doi.org/10.1093/gji/ggu224>
- Warren, L. M., Hughes, A. N., & Silver, P. G. (2007). Earthquake mechanics and deformation in the Tonga-Kermadec subduction zone from fault plane orientations of intermediate- and deep-focus earthquakes. *Journal of Geophysical Research*, 112(B5), B05314. <https://doi.org/10.1029/2006JB004677>
- Wessel, P., Luis, J. F., Uieda, L., Scharroo, R., Wobbe, F., Smith, W. H. F., & Tian, D. (2019). The generic mapping tools version 6. *Geochemistry, Geophysics, Geosystems*, 20(11), 5556–5564. <https://doi.org/10.1029/2019GC008515>
- Wiens, D. A., & Gilbert, H. J. (1996). Effect of slab temperature on deep-earthquake aftershock productivity and magnitude–frequency relations. *Nature*, 384(6605), 153–156. <https://doi.org/10.1038/384153a0>
- Wortel, R. (1982). Seismicity and rheology of subducted slabs. *Nature*, 296(5857), 553–556. <https://doi.org/10.1038/296553a0>
- Ye, L., Lay, T., Kanamori, H., Zhan, Z., & Duputel, Z. (2016). Diverse rupture processes in the 2015 Peru deep earthquake doublet. *Science Advances*, 2(6). <https://doi.org/10.1126/sciadv.1600581>
- Zahradník, J., Čížková, H., Bina, C. R., Sokos, E., Janský, J., Tavera, H., & Carvalho, J. (2017). A recent deep earthquake doublet in light of long-term evolution of Nazca subduction. *Scientific Reports*, 7, 45153. <https://doi.org/10.1038/srep45153>
- Zahradník, J., Turhan, F., Sokos, E., & Gallovič, F. (2023). Asperity-like (segmented) structure of the 6 February 2023 Turkish earthquakes. *EarthArXiv*. <https://doi.org/10.31223/XST666>
- Zhan, Z. (2017). Gutenberg–Richter law for deep earthquakes revisited: A dual-mechanism hypothesis. *Earth and Planetary Science Letters*, 461, 1–7. <https://doi.org/10.1016/j.epsl.2016.12.030>
- Zhan, Z. (2020). Mechanisms and implications of deep earthquakes. *Annual Review of Earth and Planetary Sciences*, 48(1), 147–174. <https://doi.org/10.1146/annurev-earth-053018-060314>
- Zhan, Z., & Kanamori, H. (2016). Recurring large deep earthquakes in Hindu Kush driven by a sinking slab. *Geophysical Research Letters*, 43(14), 7433–7441. <https://doi.org/10.1002/2016GL069603>
- Zhan, Z., Kanamori, H., Tsai, V. C., Helmlberger, D. V., & Wei, S. (2014). Rupture complexity of the 1994 Bolivia and 2013 Sea of Okhotsk deep earthquakes. *Earth and Planetary Science Letters*, 385, 89–96. <https://doi.org/10.1016/j.epsl.2013.10.028>
- Zhao, L.-S., & Helmlberger, D. V. (1994). Source estimation from broadband regional seismograms. *Bulletin of the Seismological Society of America*, 84(1), 91–104. <https://doi.org/10.1785/BSSA0840010091>
- Zhu, L., & Helmlberger, D. V. (1996). Advancement in source estimation techniques using broadband regional seismograms. *Bulletin of the Seismological Society of America*, 86(5), 1634–1641. <https://doi.org/10.1785/BSSA0860051634>